

2

NAVAL POSTGRADUATE SCHOOL  
Monterey, California

AD-A277 224



DTIC  
ELECTE  
MAR 25 1994  
E D

THESIS

SODIUM SULFATE CORROSION OF SILICON CARBIDE  
FIBER-REINFORCED LITHIUM ALUMINOSILICATE  
GLASS-CERAMIC MATRIX COMPOSITES

by

Leopoldo C. Maldia

December, 1993

Thesis Advisor:

Alan G. Fox

Approved for public release; distribution is unlimited.

7/10

94-09105



94 3 22 021

REPORT DOCUMENTATION PAGE			Form Approved OMB No. 0704	
Public reporting burden for this collection of information is estimated to average 1 hour per response, including the time for reviewing instruction, searching existing data sources, gathering and maintaining the data needed, and completing and reviewing the collection of information. Send comments regarding this burden estimate or any other aspect of this collection of information, including suggestions for reducing this burden, to Washington headquarters Services, Directorate for Information Operations and Reports, 1215 Jefferson Davis Highway, Suite 1204, Arlington, VA 22202-4302, and to the Office of Management and Budget, Paperwork Reduction Project (0704-0188) Washington DC 20503.				
1. AGENCY USE ONLY		2. REPORT DATE 16 December 1993		3. REPORT TYPE AND DATES COVERED Master's Thesis
4. TITLE AND SUBTITLE: Sodium Sulfate Corrosion of Silicon Carbide Fiber-Reinforced Lithium Aluminosilicate Glass-Ceramic Matrix Composites			5. FUNDING NUMBERS	
6. AUTHOR(S) Leopoldo C. Maldia				
7. PERFORMING ORGANIZATION NAME(S) AND ADDRESS(ES) Naval Postgraduate School Monterey, CA 93943-5000			8. PERFORMING ORGANIZATION REPORT NUMBER	
9. SPONSORING/MONITORING AGENCY NAME(S) AND ADDRESS(ES) Naval Air Warfare Center Warminster, PA 18974			10. SPONSORING/MONITORING AGENCY REPORT NUMBER	
11. SUPPLEMENTARY NOTES The views expressed in this thesis are those of the author and do not reflect the official policy or position of the Department of Defense or the U.S. Government.				
12a. DISTRIBUTION/AVAILABILITY STATEMENT Approved for public release; distribution is unlimited.			12b. DISTRIBUTION CODE *A	
13. ABSTRACT  Sodium sulfate hot corrosion of a SiC fiber-reinforced lithium aluminosilicate (LAS) glass-ceramic matrix composite was studied using Scanning Electron Microscope (SEM) and X-ray Diffraction (XRD). Changes in the microstructural and chemical composition of the specimens were investigated. The samples provided by Naval Air Warfare Center (NAWC), Warminster, PA were grouped as follows: (1) as-received, (2) Na <sub>2</sub> SO <sub>4</sub> salt-coated and heat-treated in oxygen, (3) noncoated and heat-treated in oxygen, (4) Na <sub>2</sub> SO <sub>4</sub> salt-coated and heat-treated in argon, and (5) noncoated and heat-treated in argon. Heat treatment was performed by NAWC for 100 hours at 900 °C. Experimental data obtained indicated that the presence of Na <sub>2</sub> SO <sub>4</sub> in an oxidative environment resulted in rapid corrosion of the matrix and SiC fibers and in the latter rings of SiO <sub>2</sub> replaced what had previously been SiC. There was very limited degradation of the fibers and matrix exposed at the surface in the noncoated sample heat-treated in oxygen and in the salt-coated sample heat-treated in argon. A significant reduction in the amount of mullite in the matrices of all heat-treated samples was observed. Mullite dissolved into either the glassy phase or into the β-spodumene matrix. Lastly, the presence of distinct magnesium silicate crystalline phases in the salt-coated and heat-treated in oxygen sample implies that the MgO at the surface reacted with the SiO <sub>2</sub> in the matrix.				
14. SUBJECT TERMS (1) SiC fiber-reinforced composites, (2) Lithium aluminosilicate glass ceramics			15. NUMBER OF PAGES: 72	
			16. PRICE CODE	
17. SECURITY CLASSIFICATION OF REPORT Unclassified	18. SECURITY CLASSIFICATION OF THIS PAGE Unclassified	19. SECURITY CLASSIFICATION OF ABSTRACT Unclassified	20. LIMITATION OF ABSTRACT UL	

Approved for public release; distribution is unlimited.

**Sodium Sulfate Corrosion of Silicon Carbide Fiber-Reinforced  
Lithium Aluminosilicate Glass-Ceramic Matrix Composites**

by

**Leopoldo C. Maldia**

**Lieutenant, United States Navy**

**B.S., University of Washington, Seattle, WA, 1984**

**Submitted in partial fulfillment  
of the requirements for the degree of**

**MASTER OF SCIENCE IN MECHANICAL ENGINEERING**

from the

**NAVAL POSTGRADUATE SCHOOL**

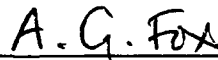
**December 1993**

Author:



Leopoldo C. Maldia

Approved by:



Alan G. Fox, Thesis Advisor



Matthew D. Kelleher, Chairman

Department of Mechanical Engineering

## ABSTRACT

Sodium sulfate hot corrosion of a SiC fiber-reinforced lithium aluminosilicate (LAS) glass-ceramic matrix composite was studied using Scanning Electron Microscope (SEM) and X-ray Diffraction (XRD). Changes in the microstructural and chemical composition of the specimens were investigated. The samples provided by Naval Air Warfare Center (NAWC), Warminster, PA were grouped as follows: (1) as-received, (2)  $\text{Na}_2\text{SO}_4$  salt-coated and heat-treated in oxygen, (3) noncoated and heat-treated in oxygen, (4)  $\text{Na}_2\text{SO}_4$  salt-coated and heat-treated in argon, and (5) noncoated and heat-treated in argon. Heat treatment was performed by NAWC for 100 hours at 900 °C. Experimental data obtained indicated that the presence of  $\text{Na}_2\text{SO}_4$  in an oxidative environment resulted in rapid corrosion of the matrix and SiC fibers and in the latter rings of  $\text{SiO}_2$  replaced what had previously been SiC. There was very limited degradation of the fibers and matrix exposed at the surface in the noncoated sample heat-treated in oxygen and in the salt-coated sample heat-treated in argon. A significant reduction in the amount of mullite in the matrices of all heat-treated samples was observed. Mullite dissolved into either the glassy phase or into the  $\beta$ -spodumene matrix. Lastly, the presence of distinct magnesium silicate crystalline phases in the salt-coated and heat-treated in oxygen sample implies that the MgO at the surface reacted with the  $\text{SiO}_2$  in the matrix.

## TABLE OF CONTENTS

I. INTRODUCTION . . . . .	1
II. BACKGROUND . . . . .	3
A. GLASS CERAMICS . . . . .	3
B. THE LITHIUM ALUMINOSILICATE SYSTEM . . . . .	4
C. SiC FIBER-REINFORCED LAS COMPOSITES . . . . .	7
D. CORROSION OF SiC/LAS COMPOSITES BY Na <sub>2</sub> SO <sub>4</sub> . . . . .	11
III. SCOPE OF PRESENT WORK . . . . .	19
IV. EXPERIMENTAL PROCEDURE . . . . .	20
A. SCANNING ELECTRON MICROSCOPY . . . . .	23
B. X-RAY DIFFRACTION . . . . .	24
V. RESULTS AND DISCUSSION . . . . .	26
A. OPTICAL AND SCANNING ELECTRON MICROSCOPY (SEM) . . . . .	26
B. X-RAY DIFFRACTION (XRD) ANALYSIS . . . . .	40

VI. CONCLUSIONS . . . . .	55
VII. RECOMMENDATIONS . . . . .	56
LIST OF REFERENCES . . . . .	58
INITIAL DISTRIBUTION LIST . . . . .	61

Accession For	
NTIS CRA&I	<input checked="" type="checkbox"/>
DTIC TAB	<input type="checkbox"/>
Unannounced	<input type="checkbox"/>
Justification .....	
By .....	
Distribution / .....	
Availability Codes	
Dist	Avail and/or Special
A-1	

## LIST OF TABLES

TABLE I.	COMPOSITION OF SiC/LAS COMPOSITE . . . .	23
TABLE II.	CRYSTALLINE PHASES PRESENT, RELATIVE INTENSITIES, MILLER INDICES, AND $2\theta$ LOCATIONS OF PEAKS IN THE AS-RECEIVED SAMPLE . . . .	47
TABLE III.	SELECTED $\beta$ -SPODUMENE PEAK INTENSITIES IN AS- RECEIVED AND SALT-COATED SAMPLES HEAT-TREATED IN OXYGEN . . . . .	53

## LIST OF FIGURES

<b>Figure 1.</b>	The lithium-alumino-silicate system phase diagram . . . . .	5
<b>Figure 2.</b>	Longitudinal thermal expansion of beta-spodumene solid solution . . . . .	6
<b>Figure 3.</b>	Volume expansion of beta-spodumene . . . . .	7
<b>Figure 4.</b>	Flexural strength of monolithic LAS ceramic and SiC/LAS composites . . . . .	8
<b>Figure 5.</b>	Fracture toughness of monolithic LAS ceramic and SiC/LAS composites . . . . .	9
<b>Figure 6.</b>	SEM micrograph showing crack impediment by SiC fiber . . . . .	10
<b>Figure 7.</b>	Schematic representation of SiO <sub>2</sub> layer . . . . .	12
<b>Figure 8.</b>	Corrosion region as a function of reciprocal temperature and oxidant pressure . . . . .	14
<b>Figure 9.</b>	Na <sub>2</sub> SO <sub>4</sub> deposition dewpoints . . . . .	15
<b>Figure 10.</b>	Stress-strain curves of SiC/LAS tensile samples . . . . .	17
<b>Figure 11.</b>	Glass slurry infiltration process . . . . .	20
<b>Figure 12.</b>	Optical microscope image of as-received sample . . . . .	26
<b>Figure 13.</b>	BS electron SEM micrograph of as-received specimen matrix . . . . .	28
<b>Figure 14.</b>	EDX spectra of mullite and beta-spodumene matrix . . . . .	29
<b>Figure 15.</b>	BS electron SEM image of zircon crystalline phases . . . . .	30
<b>Figure 16.</b>	Comparison of extent of corrosion in salt-coated and noncoated samples heat-treated in oxygen . . . . .	31



Figure 17.	BS electron SEM image of magnesium silicate phase . . . . .	34
Figure 18.	EDX spectra of magnesium silicate phase . .	35
Figure 19.	Secondary electron SEM image and x-ray elemental map of oxidized SiC fiber . . . . .	37
Figure 20.	BS electron SEM topographic image of oxidized SiC fiber . . . . .	38
Figure 21.	BS electron SEM images of salt-coated and noncoated samples heat-treated in argon . .	39
Figure 22.	XRD patterns of as-received specimen . . . .	41
Figure 23.	XRD patterns of as-received specimen and two LAS polymorphs . . . . .	44
Figure 24.	$\text{Li}_2\text{O}-\text{Al}_2\text{O}_3-\text{SiO}_2$ ternary phase diagram . . . .	45
Figure 25.	XRD patterns of as-received sample and two SiC polymorphs . . . . .	46
Figure 26.	XRD patterns of as-received, salt-coated and noncoated samples heat-treated in oxygen . .	49
Figure 27.	XRD patterns of as-received, salt-coated and noncoated samples heat-treated in argon . .	50
Figure 28.	BS electron SEM images of as-received and heat-treated samples . . . . .	51

## **ACKNOWLEDGEMENTS**

I would like to express my sincere appreciation to my thesis advisor Professor Alan G. Fox for his guidance and assistance in helping me complete this thesis. Nobody could have asked for a better thesis advisor.

I dedicate this thesis to my family ... my constant source of joy and support throughout the entire time I spent at Naval Postgraduate School. To my daughters Niki and Krissy who never quite understood why I spent so much time at school. Last and foremost, to my beautiful wife Lorna for all the love, caring and understanding she has unselfishly given me through the years.

## I. INTRODUCTION

In order to improve the efficiency, reliability, performance and reduce the cost of gas turbine engines currently used by the U. S. Navy, SiC fiber-reinforced lithium aluminosilicate (SiC/LAS) glass-ceramic matrix composites are being considered as a replacement material for nickel-based superalloys used in gas turbine engine components. Metal superalloys are often of high density which contributes to high stresses on rotating parts. The high density also contributes to a higher overall engine weight thus decreasing the thrust to weight ratio. Additionally, current design attempts to increase gas turbine efficiency involves increasing the turbine operating temperature beyond that sustainable by metal superalloys. SiC/LAS ceramic composites offer the advantages of being lightweight (about one-third the density of metal superalloys), having a very low coefficient of thermal expansion (CTE), and maintaining toughness, strength, and resistance to corrosion at elevated temperatures.

Unfortunately, aircraft and marine gas turbine engines are often exposed to hostile operating environments. All fuels contain some amount of sulfur and sodium-containing airborne contaminants can combine with the sulfur in the fuel to form  $\text{Na}_2\text{SO}_4$  salt deposits which could accumulate on engine

components. Sodium sulfate can apparently flux the glassy components of the LAS and lead to degradation of mechanical properties.

The hot corrosion process of silicon-based ceramics has been extensively studied. However, there is very little information available on the hot corrosion behavior of SiC/LAS glass-ceramic matrix composites caused by  $\text{Na}_2\text{SO}_4$ . Successful utilization of SiC/LAS in gas turbine engines would require a thorough understanding of the corrosion process involved.

The focus of this study is on the effects of hot corrosion by sodium sulfate salt on the microstructure and chemical composition of SiC fiber-reinforced lithium aluminosilicate glass-ceramic matrix composites.

## II. BACKGROUND

### A. GLASS CERAMICS

Glass ceramics are partially crystalline, partially noncrystalline (glassy) materials formed by controlled crystallization of suitable base glasses. Properties of glass ceramics are determined primarily by the percentages of crystalline and noncrystalline phases, crystal size and distribution throughout the bulk of the material, and the crystalline and glass interface bond strength. The crystalline phase usually occupies the greater portion of the volume of the material (~ 50-100 vol.%) and its physical and chemical properties have the greatest influence on the glass ceramic properties as a whole. The increased strength of glass-ceramic materials is attributed to the fine grain and uniform microstructure. Results of studies conducted [Ref. 1] demonstrated that lithium aluminosilicate glass ceramics (63.5 wt.%  $\text{SiO}_2$ , 18.9 wt.%  $\text{Al}_2\text{O}_3$ , 5.3 wt.%  $\text{Li}_2\text{O}$  as the main components) having average crystal size of 10 microns displayed a bending strength of 86 MPa, whereas one of similar composition, but with average crystal size of 15 microns has bending strength of only 29 MPa. The bending strength of LAS glass ceramics can be as high as 274 MPa with an appropriate crystallite size and glass content.

Even though glass ceramics exhibit high strength, they are brittle at room temperature and do not exhibit ductility and plasticity common to metals. They behave as elastic substances up to the strain that produces the breakage. It has been suggested [Ref. 2] that this brittle behavior is due to the fact that the dislocations cannot move easily which results from large Burger vectors, the presence of a few slip systems, and the need to break strong ionic bonds during the slip process. Since slip and plastic deformation are unlikely to occur in glass-ceramic materials, any crack that develops is not hindered by the deformation of the material ahead of that crack. Instead, the crack continues to propagate.

#### **B. THE LITHIUM ALUMINOSILICATE SYSTEM**

The phase diagram of the lithium-alumino-silicate system is shown in Figure 1 [Ref. 1]. The important crystalline phases in the LAS system are eucryptite( $\text{Li}_2\text{O} \cdot \text{Al}_2\text{O}_3 \cdot 2\text{SiO}_2$ ),  $\beta$ -spodumene ( $\text{Li}_2\text{O} \cdot \text{Al}_2\text{O}_3 \cdot 4\text{SiO}_2$ ) and petalite( $\text{Li}_2\text{O} \cdot \text{Al}_2\text{O}_3 \cdot 8\text{SiO}_2$ ).

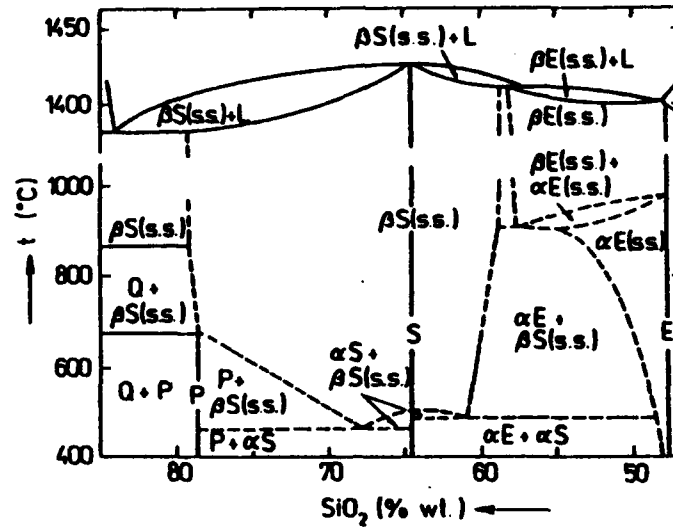
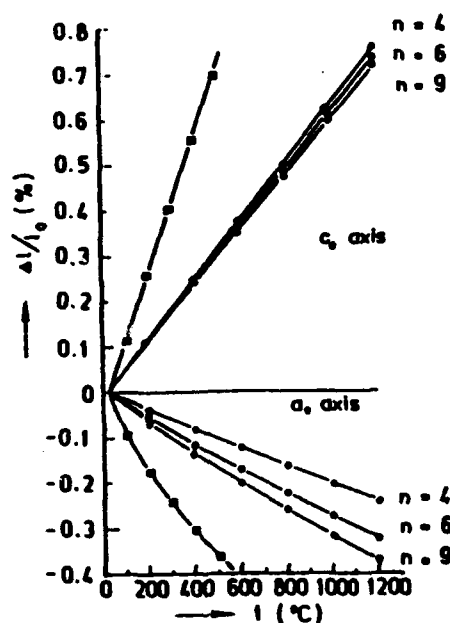


Figure 1. LAS Phase Diagram. P=petalite, E=eucryptite, Q=quartz, S=spodumene, s.s.=solid solution, L=liquid [Ref. 1].

From the diagram it can be seen that the low-temperature form of  $\alpha$ -spodumene is transformed into the high-temperature, stable form of  $\beta$ -spodumene at around 500 °C. During crystallization the stable form of  $\beta$ -spodumene crystallizes out at about 900 °C.

The most important property of  $\beta$ -spodumene is its ultra-low, zero, or even negative coefficient of thermal expansion (CTE). This property can be tailored to meet specific application temperatures, that is, the desired CTE value can be adjusted by controlling the crystallization conditions. The low CTE value is attributed to the strong anisotropy of the longitudinal expansion factor. In the  $\beta$ -spodumene tetragonal structure, as temperature increases there is

longitudinal expansion along the crystalline axis  $c_0$  and a contraction along the  $a_0$  axis. The net result is a very low overall expansion. An important factor that affects CTE is the amount of  $\text{SiO}_2$  in the  $\beta$ -spodumene solid solution as shown in Figure 2. CTE increases with decreasing  $\text{SiO}_2$  content in solid solutions of  $\beta$ -spodumene.



**Figure 2.** Longitudinal thermal expansion of solid solutions of  $\beta$ -spodumene in the  $a_0$  and  $c_0$  crystallographic directions. [Ref. 1]

Figure 3 shows the volume expansion of solid solutions of  $\beta$ -spodumene as a function of  $\text{SiO}_2$  content. As the  $\text{SiO}_2$  content decreases there is a corresponding increase in volume expansion.



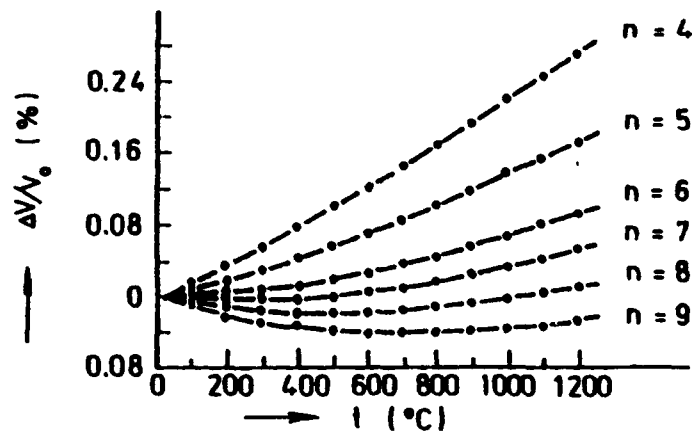


**Figure 3.** Volume Expansion of  $\beta$ -spodumene ( $\text{Li}_2\text{O} \cdot \text{Al}_2\text{O}_3 \cdot n\text{SiO}_2$ ) [Ref. 1]

The low coefficient of thermal expansion of  $\beta$ -spodumene glass ceramics becomes an important factor in determining the resistance of the material to thermal shock. Studies conducted [Ref. 1] showed that glass ceramics plates (600 x 600 x 5 mm) having  $\beta$ -spodumene as the main crystalline phase with a CTE of  $3.3 \times 10^{-7} \text{ K}^{-1}$  (25-700 °C) can be cooled from 700 °C to 0 °C without any damage.

Other important properties of LAS glass ceramics are high elastic moduli, high melting points, and high resistance to oxidation at elevated temperatures.

### C. SiC FIBER-REINFORCED LAS COMPOSITES

SiC fiber-reinforced LAS matrix composites are prospective materials for high temperature structural applications. These composites maintain the high elastic moduli, high melting

point, and high-temperature oxidation resistance of the parent glass ceramics. The fracture toughness of LAS matrix is remarkably improved by fiber reinforcement to the point that they approach the values of some metals. The fibers themselves exhibit high strength and toughness. Fiber properties of Nicalon (Nippon Carbon Co.) fiber show an average strength of 2480-3240 MPa and average modulus of elasticity of 180-200 GPa [Ref. 3].

Figures 4 and 5 demonstrate the improvement in flexural strength and fracture toughness, respectively, of SiC/LAS composites (50 vol.% SiC fiber) over monolithic ceramics.

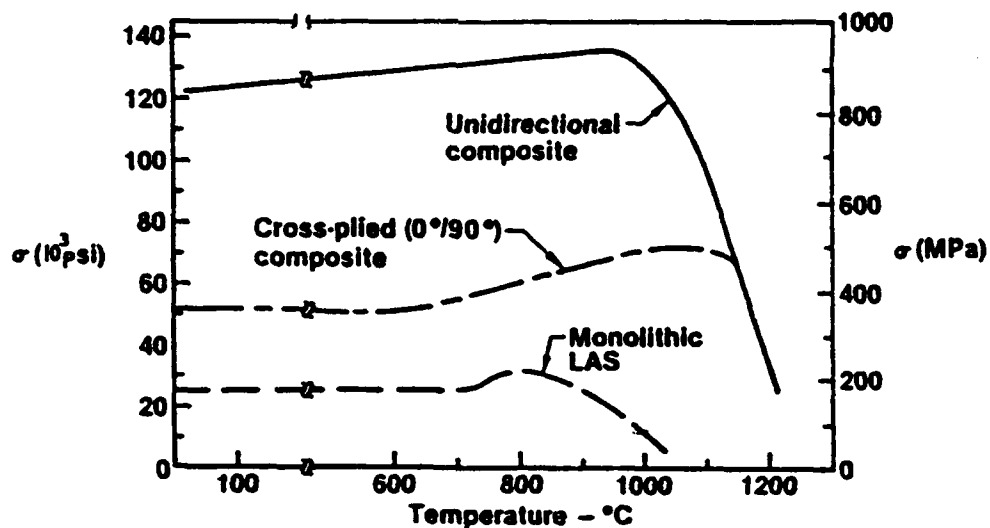
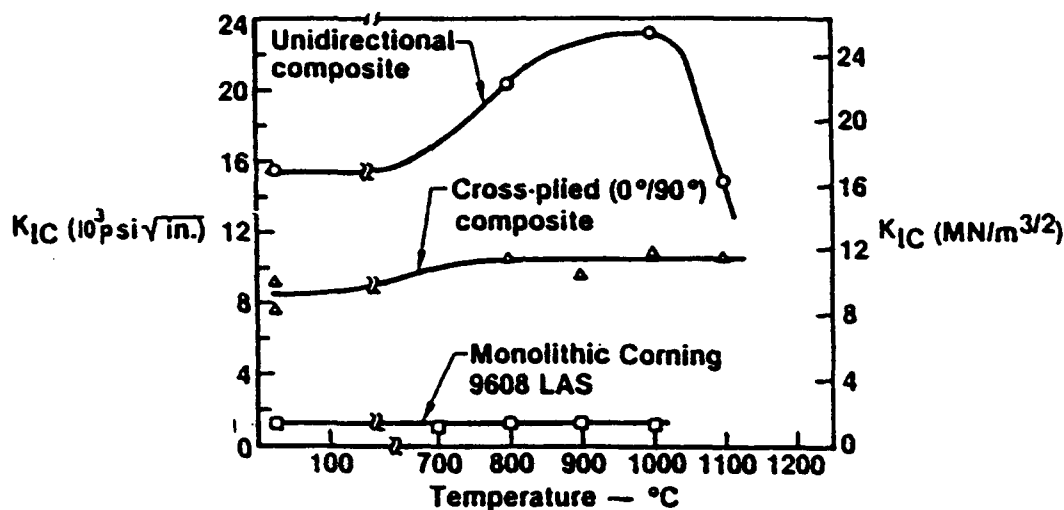


Figure 4. Flexural strength of monolithic LAS ceramic, cross-plyed, and unidirectional SiC/LAS composites over a range of temperatures [Ref. 4].

Noteworthy from Figure 4 is the fact that at around 1000 °C monolithic LAS ceramics have very little useful strength, whereas unidirectional and cross-plyed composites are at their peak values.



**Figure 5.** Fracture toughness of monolithic LAS ceramics, cross-plyed and unidirectional LAS/SiC composites [Ref. 4].

The most impressive mechanical property of SiC fiber-reinforced LAS is fracture toughness as shown in Figure 5. At around 1000 °C, the fracture toughness of cross-plyed composite is about 10 times that of monolithic ceramics; and unidirectional composite is about 23 times more fracture tough than monolithic ceramics. These  $K_{IC}$  values are just slightly less than those typical of some aluminum alloys.

Strengthening of the composite by the SiC fibers is achieved mainly through the mechanism of load transfer from

the matrix to the fibers in shear. The load transfer shifts the stress from the matrix to the relatively long, high modulus fibers. Also, the fibers impede crack propagation through the matrix material [Ref. 2] as shown in Figure 6.

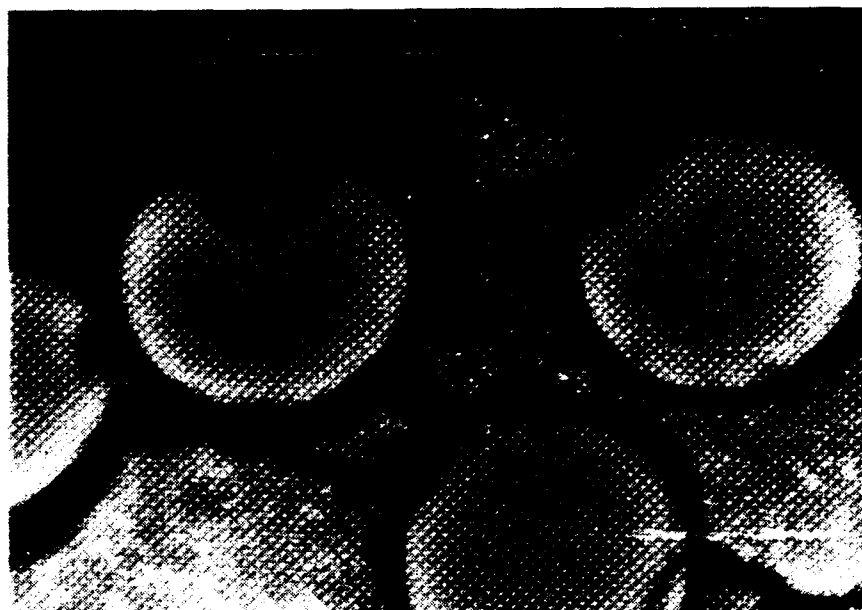


**Figure 6.** SEM micrograph showing SiC fibers impeding crack propagation through the LAS matrix.

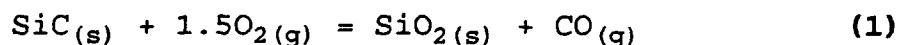
The remarkable improvement in fracture toughness has been attributed to fiber-matrix debonding, fiber pull-out from the matrix, crack deflection, and crack impediment. It has been suggested [Ref. 5] that the degree of cohesion between the fiber and the matrix plays an important role in the toughness of fiber-reinforced composites. When either the chemical bonding at the fiber-matrix interface is too strong or the radial stresses imparted by the matrix to the fiber is too high, there will be a resultant increase in strength, but the

composite will fail abruptly. On the other hand, if there is no chemical bonding or frictional forces between the fiber and the matrix there will be no load transfer from the matrix to the fiber resulting to decreased strength and toughness of the composite. Obtaining optimum cohesion at the matrix-fiber interface is critical to composite toughness and strength.

The interface between the SiC fiber and the matrix was observed to be an amorphous, carbon-rich layer approximately 70-170 nm wide [Ref. 6]. This C-rich layer forms during the fabrication process, i.e., hot pressing, from the chemical reaction  $\text{SiC}_{(s)} + \text{O}_{2(g)} \rightarrow \text{SiO}_{2(s)} + \text{C}_{(s)}$ . The carbon layer itself is about 20-50 nm. The carbon forms a coating around the fiber which facilitates optimal bonding at the interface.

#### D. CORROSION OF SiC/LAS COMPOSITES BY $\text{Na}_2\text{SO}_4$

Before discussing the mechanism of corrosion by  $\text{Na}_2\text{SO}_4$  it is important to have an understanding of the silica ( $\text{SiO}_2$ ) protective layer around the SiC fibers. SiC is inherently unstable in air. In an oxidizing environment, SiC reacts with the oxygen to form the protective layer  $\text{SiO}_2$  which is analogous to the protective coating  $\text{Al}_2\text{O}_3$  in aluminum alloys. It is generally accepted that the oxidation of SiC in a fuel-lean environment involves the following reaction:



The protective layer is shown schematically in Figure 7 [Ref. 8].

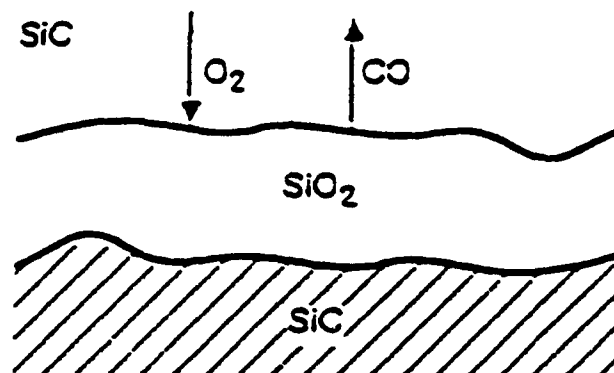
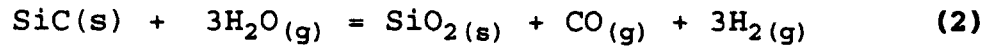


**Figure 7.** Schematic representation of SiO<sub>2</sub> layer [Ref. 8].

Among the common oxides, SiO<sub>2</sub> has the lowest permeability to oxygen. Hence, SiO<sub>2</sub> forms an effective oxidation reaction barrier by restricting oxygen diffusion into the SiO<sub>2</sub>-SiC interface [Ref. 8, 17]. It is commonly accepted that oxygen rather than Si is the mobile species in the oxidation of SiC. It then follows that the chemical reaction must occur at the SiO<sub>2</sub>/SiC or SiO<sub>2</sub>/matrix interface. The movement through SiO<sub>2</sub> takes place by diffusion of molecular oxygen as interstitial or by network exchange of ionic oxygen. Since the diffusion coefficient of molecular oxygen is about 10<sup>6</sup> times that of ionic oxygen, oxygen transport must occur by molecular oxygen diffusion [Ref. 8].

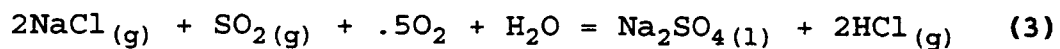
In a fuel-rich environment, H<sub>2</sub>O gas is one of the byproducts of combustion and oxidation of SiC takes the following form:



It has been demonstrated by Deal and Grove [Ref. 7] that the oxidation of SiC is over an order of magnitude faster in wet O<sub>2</sub> than in a dry environment due to the fact that H<sub>2</sub>O has a higher solubility in SiO<sub>2</sub> (~3.4 x 10<sup>19</sup> molecules/cm<sup>3</sup>) compared to solubility of molecular oxygen in SiO<sub>2</sub> (~5.5 x 10<sup>16</sup> molecules/cm<sup>3</sup>). Thus, the rapid permeation of H<sub>2</sub>O molecules results to the accelerated oxidation of SiC. This one of the reasons why gas turbine engines are normally operated in the fuel-lean region.

The effectiveness of SiO<sub>2</sub> as a protective oxide is limited by its melting point (2000 K). Once SiO<sub>2</sub> has liquified, it begins to flow such that it facilitates the rapid transport and oxidation rates. Also, at sufficiently high temperatures, SiC and SiO<sub>2</sub> react to give SiO and CO gases thus generating gas pressure at the interface [Ref. 8].

Potential applications of SiC/LAS composite materials as gas turbine engine hot section components, i.e., combustor liner, disks, and possibly turbine blades involve exposure of the components to combustion gases and deposit-forming corrodents. The most common form of deposit is sodium sulfate (Na<sub>2</sub>SO<sub>4</sub>) which forms when the sodium from the environment reacts with the sulfur fuel impurities. The reaction is given by:



Sodium sulfate is a highly stable salt, and it forms a deposit on engine components. It is suggested [Ref. 8] that deposit-induced corrosion (also called "hot corrosion") occurs in two steps: (1) deposition of sodium sulfate salt and (2) corrosive attack. Sodium sulfate is considered corrosive between its melting point (1157 K) and the dewpoint at which sodium sulfate deposit forms. Although the region in which  $\text{Na}_2\text{SO}_4$  becomes corrosive is very limited, as shown in Figure 8, it can be very severe.

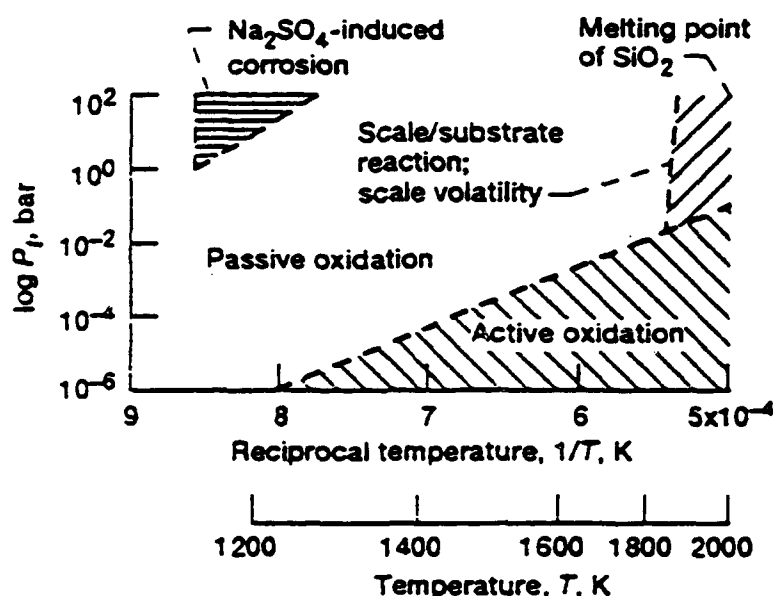


**Figure 8.** Corrosion region as a function of reciprocal temperature and oxidant pressure [Ref. 8].

Also shown in Figure 9, as the pressure increases so does the dewpoint which means that the corrosive region likewise expands. Potential applications of LAS/SiC composites are in



the area of gas turbine engines that will operate at higher temperatures and pressures. Higher temperature diminishes the occurrence of  $\text{Na}_2\text{SO}_4$  deposition because the dewpoint temperature will be exceeded. However, higher pressures mean that the dewpoint temperature will also increase. Knowing the engine operating parameters is, therefore, essential in determining whether  $\text{Na}_2\text{SO}_4$  deposits will form or not.

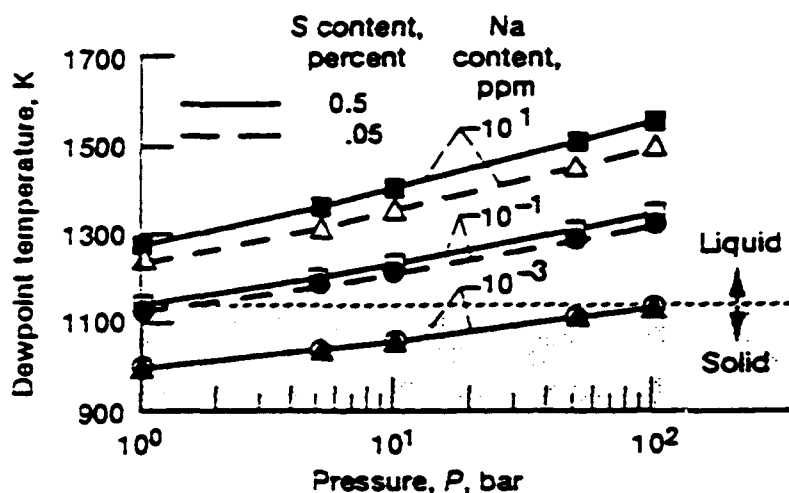
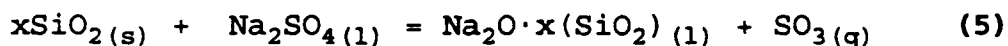
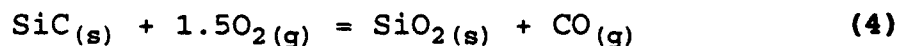


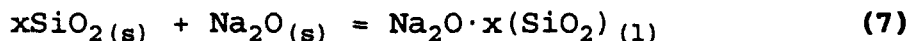
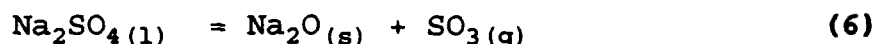
Figure 9.  $\text{Na}_2\text{SO}_4$  deposition dewpoints [Ref. 8].

The key chemical reactions in hot corrosion by  $\text{Na}_2\text{SO}_4$  are:



The protective  $\text{SiO}_2$  solid layer is transformed to a liquid scale which accelerates the corrosive attack due to increased transport through the liquid [Ref. 8].

Equation (5) can be written in terms of acid-base reactions:



$\text{SiO}_2$  is an acidic oxide and, in accordance with the Lewis' concept of acid-base reaction, it reacts with the basic oxide  $\text{Na}_2\text{O}$  forming the salt sodium silicate ( $\text{Na}_2\text{O} \cdot \text{SiO}_2$ ). The partial pressure of  $\text{SO}_3$  ( $P_{\text{SO}_3}$ ) plays an important role in determining the formation of sodium silicate salt.  $\text{Na}_2\text{SO}_4$  is a basic molten salt when it has a high activity of  $\text{Na}_2\text{O}$  resulting from a low  $P_{\text{SO}_3}$ . At high  $P_{\text{SO}_3}$ ,  $\text{Na}_2\text{SO}_4$  is acidic and it does not react with acidic  $\text{SiO}_2$  oxide. Jacobson [Ref. 8, 9] verified these predictions by treating test coupons in a burner rig using both low- and high-sulfur fuels. More corrosion was observed on samples exposed to low-sulfur (low  $P_{\text{SO}_3}$ ) than those exposed to high-sulfur fuels. Additionally, no sodium silicate was detected in the latter.

Many types of SiC fibers have excess carbon which makes them highly susceptible to corrosion. Carbon tends to drive  $\text{Na}_2\text{SO}_4$  basic such that, even in conditions where  $P_{\text{SO}_3}$  is high enough to limit the reaction between  $\text{Na}_2\text{SO}_4$  and  $\text{SiO}_2$ , corrosion can still be quite extensive. Oxygen pressure is another factor that affects corrosion. It has been shown that high oxygen pressure drives  $\text{Na}_2\text{SO}_4$  acidic enough that dissolution of  $\text{SiO}_2$  does not occur.

Thus, based on Lewis' concept of acid-base reactions alone, the hot corrosion regimes of  $\text{Na}_2\text{SO}_4$  can be predicted.

Previous work by Kowalik, Wang, and Sands [Ref. 16] on sodium sulfate corrosion of SiC/LAS glass-ceramic composites demonstrated that hot corrosion by  $\text{Na}_2\text{SO}_4$  resulted in about 30% reduction in tensile strength of samples coated with the salt and heat-treated in oxygen. As shown in Figure 10 the as-received sample has the highest failure strength whereas the salt-coated sample heat-treated in the presence of oxygen has the lowest value. Failure strength values of samples heat-treated in argon (both coated and noncoated) fall in between the two.

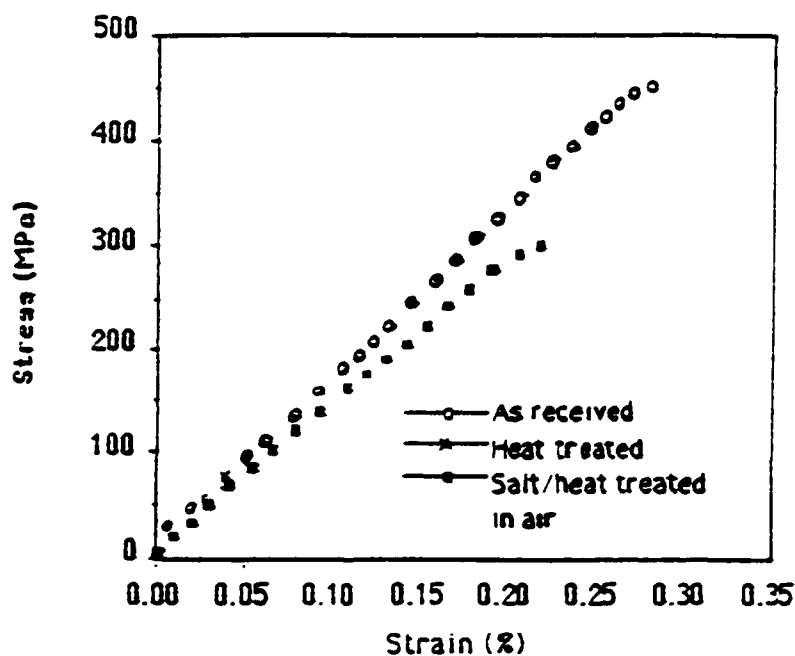


Figure 10. Stress-strain curves of SiC/LAS tensile samples [Ref. 16].

Kowalik, et. al concluded that the presence of sodium sulfate in an oxidizing atmosphere resulted in rapid degradation of the SiC fibers and that the Na reacted with the  $\text{SiO}_2$  and lowered its viscosity. The lowering of the viscosity further enhanced the diffusion of oxygen in the glass.

### III. SCOPE OF PRESENT WORK

Based upon previous work and literature review presented in this paper, it is evident that hot corrosion by sodium sulfate resulted in rapid oxidation of SiC fibers in fiber-reinforced LAS composites which lead to the degradation of mechanical properties.

The present work involved the investigation of the microstructural and chemical changes in the fibers and matrix of SiC/LAS glass-ceramic matrix composites exposed to sodium sulfate and heat-treated in various environments. The samples studied were provided by Naval Air Warfare Center (NAWC), Warminster, PA and were grouped as follows: (1) as-received, (2) salt-coated and heat-treated in oxygen, (3) noncoated and heat-treated in oxygen, (4) salt-coated and heat-treated in argon, and (5) noncoated and heat-treated in argon. NAWC performed the heat treatment at 900 °C for 100 hours. Scanning Electron Microscope (SEM) and X-ray Diffraction (XRD) were employed in the analyses of the samples.

#### IV. EXPERIMENTAL PROCEDURE

The ceramed SiC/LAS composite was fabricated by United Technologies Research Center, East Hartford, Connecticut. Figure 11 is a simplified representation of the fabrication process.

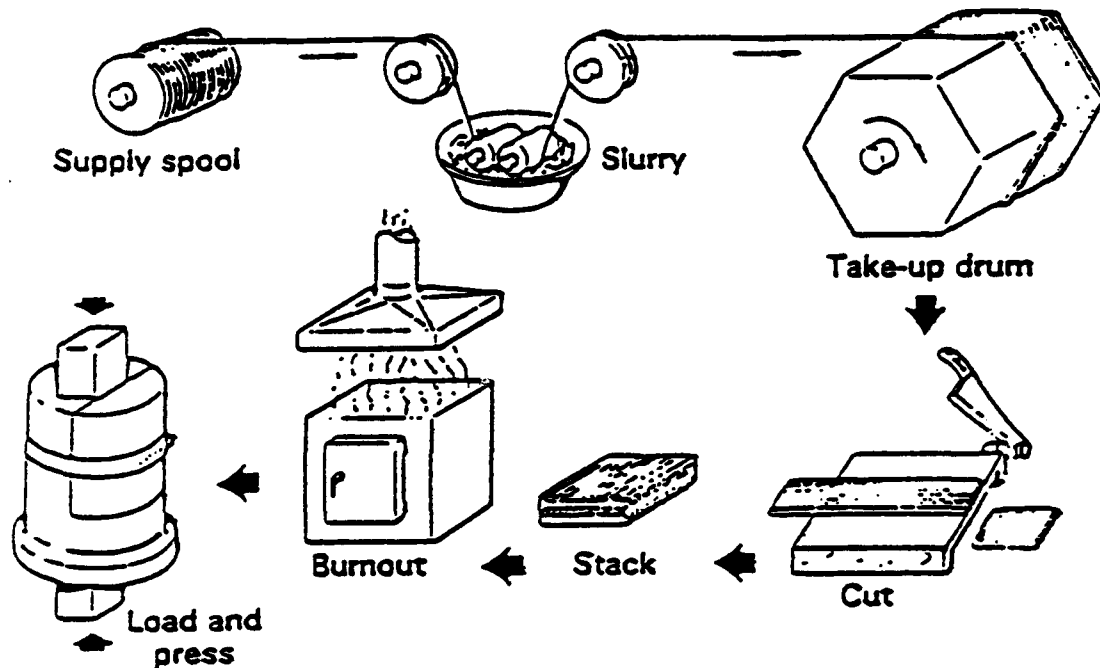


Figure 11. Glass slurry infiltration process [Ref. 22]

The fabrication process involves the following steps:

1. Impregnation of Nicalon SiC yarn with the glass powder slurry. The glass powder contains  $\text{MgO}$ ,  $\text{SiO}_2$ ,  $\text{Li}_2\text{CO}_3$ ,  $\text{Al}_2\text{O}_3$  which were melted, homogenized, quenched in cold water, and pulverized with a  $\text{ZrO}_2$  ball mill.  $\text{SiO}_2$ ,  $\text{Li}_2\text{CO}_3$ , and  $\text{Al}_2\text{O}_3$  are the main constituents of the LAS glass.  $\text{MgO}$  modifies the phase composition and microstructure while  $\text{ZrO}_2$  serves as the nucleating agent during crystallization. Other components added were  $\text{As}_2\text{O}_3$  as a refining agent and  $\text{BaO}$  which lowers glass melting point.  $\text{B}_2\text{O}_3$  was incorporated with the powder to form a boron/carbon layer around the fiber to reduce oxidation [Ref. 10]. Organic compounds such as defoamers, plasticizers, and binders are added to the aqueous glass slurry.
2. Controlled wrapping of the impregnated yarn on to a mandrel.
3. Tapes are dried and removed from mandrel and cut into desired sizes.
4. Tapes are stacked into desired fiber orientation and placed in a furnace at  $600^\circ\text{C}$  for 30 minutes to burn off the organic compounds.
5. Stacks are hot-pressed under vacuum at  $125^\circ\text{C}$ .
6. Crystallize (ceram) at  $900^\circ\text{C}$  for 24 hours.

The five specimens of SiC/LAS ceramic composites used in this study were provided by Dr. S. Wang, Aircraft Division, Naval Air Warfare Center, Warminster, PA. The five samples were categorized as follows:

1. As-received.
2. No salt coating, heat treated at  $900^\circ\text{C}$  for 100 hours in flowing oxygen.
3. No salt coating, heat treated at  $900^\circ\text{C}$  for 100 hours in flowing argon.

4. Coated with  $\text{Na}_2\text{SO}_4$  and heat treated at 900 °C for 100 hours in flowing oxygen.
5. Coated with  $\text{Na}_2\text{SO}_4$  and heat treated at 900 °C for 100 hours in flowing argon.

The as-received sample was used to provide baseline information for the microstructural and chemical analyses. The second and third samples provided information on the effects of heat treatment in oxygen and argon environments. The fourth and fifth specimens showed the effects of  $\text{Na}_2\text{SO}_4$  on the hot corrosion of the composite. The salt-coated specimens have approximately 3.0 mg/cm<sup>2</sup> coating of  $\text{Na}_2\text{SO}_4$  which is equivalent to the  $\text{Na}_2\text{SO}_4$  deposit on gas turbine engine components operating at 900 °C for 500 hours having a sulfur fuel impurity of 0.05% [Ref. 11, 16]. Only one side of the salt-coated test coupons was coated with  $\text{Na}_2\text{SO}_4$ .

The samples examined consisted of three plies of continuous unidirectional Nicalon SiC fibers. The composition of SiC/LAS composite is provided in TABLE I.



TABLE I. COMPOSITION OF SiC/LAS COMPOSITE

OXIDE COMPONENTS	COMPOSITION(wt.%)
$\text{Li}_2\text{O}$	3.2
$\text{Al}_2\text{O}_3$	20.0
$\text{SiO}_2$	67.5
$\text{MgO}$	2.5
$\text{BaO}$	1.2
$\text{As}_2\text{O}_3$	1.0
$\text{B}_2\text{O}_3$	3.1
$\text{ZrO}_2$	1.5

#### A. SCANNING ELECTRON MICROSCOPY

The specimens were mounted on Conductive Phenolic Mounting Compound (Konductomet I) in such a way that the sample cross-section showed a  $90^\circ/0^\circ/90^\circ$  fiber orientation. This facilitated the examination of the salt-coated sides. The samples were then ground and finally polished to 0.05 micron using 30% Gamma Alumina suspension. In order to make the specimens conducting for the scanning electron microscope (SEM) analysis, each sample was coated with carbon using a vacuum evaporator. Microstructural and chemical analyses were performed using the Cambridge S200 SEM and the Kevex x-ray

Energy Dispersive Spectrometer (EDS) with an ultra thin window light element detector. In order to study the extent of diffusion of oxygen into the matrix and SiC fiber and determine the chemistry of the phases present, elemental profiles were obtained using the EDS Advanced Imaging feature. Visual examination of the phases present and taking of micrographs were accomplished using the SEM backscattered (BS) imaging method. Backscattered electrons provided improved detection of phases present using atomic number contrast [Ref. 12].

#### **B. X-RAY DIFFRACTION**

X-ray diffraction patterns of each sample were obtained using a Phillips XRG 3100 X-ray Generator and a PW 1710 Diffractometer Controller in conjunction with a Digital 3100 VAX workstation. The X-ray generator employs a copper target (Cu-K $\alpha$  1 and 2 with wavelengths equal to 1.54060 and 1.54439 angstroms, respectively) and a bent graphite crystal monochromator. Raw data were collected at a power setting of 30 KV and 35 mA. The scan program was set at an angle range of 10-90 degrees and a scan rate of 5 seconds for every 0.02 degree increment.

Raw data files for each specimen were analyzed using the VAX workstation and the Phillips APD1700 software package.

Peak positions ( $2\theta$ ) and integrated intensities were calculated, recorded, and curve-fitted for each sample. From the Phillips PW 1891 Total Access Diffraction Database (TADD) a known intensity profile for any particular compound can be recalled and compared to the specimen's X-ray diffraction patterns. With the aid of the TADD and the JCPDS X-ray Diffraction data cards, the compounds present in the sample can be identified.

## V. RESULTS AND DISCUSSION

### A. OPTICAL AND SCANNING ELECTRON MICROSCOPY (SEM)

A low magnification optical micrograph of the as-received specimen (Figure 12) shows the  $90^\circ/0^\circ/90^\circ$  fiber orientation in the composite. The specimen is characterized by a uniform spatial distribution of SiC fibers except for a few matrix-rich regions.

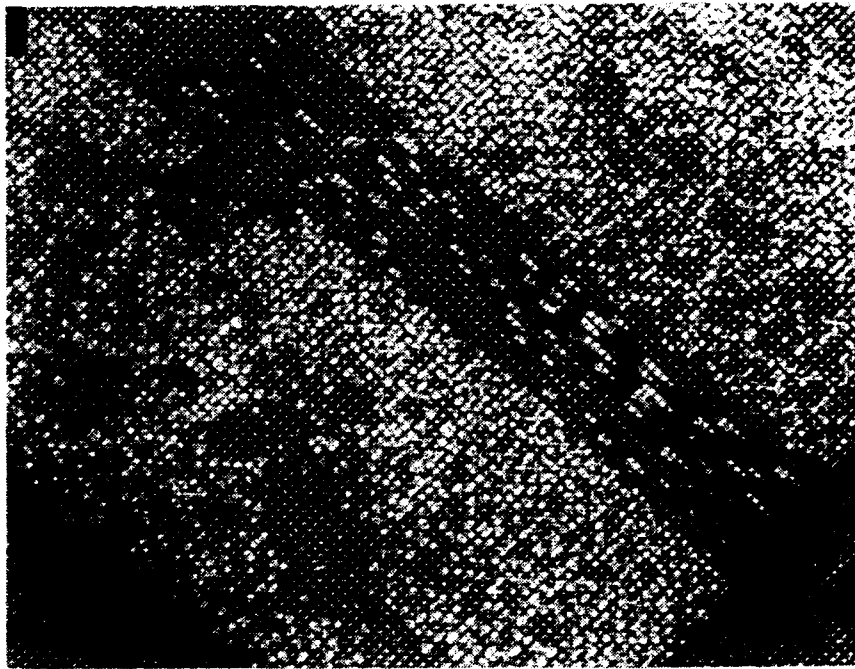


Figure 12. Optical microscope image of as-received sample at x100 magnification.

A higher magnification backscattered electron micrograph shown in Figure 13 reveals a surface morphology having a dense matrix with distinct microstructures. The elongated, light-colored phase was determined to be mullite ( $3\text{Al}_2\text{O}_3 \cdot 2\text{SiO}_2$ ) from SEM and XRD analyses. The mullite phase appears lighter than the surrounding matrix because it is a heavier compound. The EDX spectra shown in Figure 14 clearly demonstrate the fact that the mullite phase is aluminum-rich compared to the surrounding  $\beta$ -spodumene phase. This is as expected since there is a 3:1 aluminum to silicon atomic ratio in mullite and a 1:2 ratio in  $\beta$ -spodumene. Also, the  $\text{Li}_2\text{O} \cdot \text{Al}_2\text{O}_3 \cdot \text{SiO}_2$  ternary phase diagram (Figure 27 under XRD results) predicts mullite for the given composition in TABLE I. X-ray diffraction (XRD) analysis further confirmed the presence of the mullite crystalline phase. The fine, granule-like microstructures which appear the brightest (indicating the presence of heavier elements) are most likely zircon ( $\text{ZrO}_2 \cdot \text{SiO}_2$ ) and zirconia ( $\text{ZrO}_2$ ) crystalline phases. XRD analysis performed indicates the presence of small amount of zircon ( $\text{ZrO}_2 \cdot \text{SiO}_2$ ) and zirconia ( $\text{ZrO}_2$ ) (most likely tetragonal polymorph). Zirconia, present in the  $\text{ZrO}_2$  ball mill and in zirconia ( $\text{ZrO}_2$ ) which was used as a nucleating agent, appears to be distributed throughout the matrix.



**Figure 13.** Backscattered electron micrograph of as-received specimen matrix. Note the needle-like mullite.

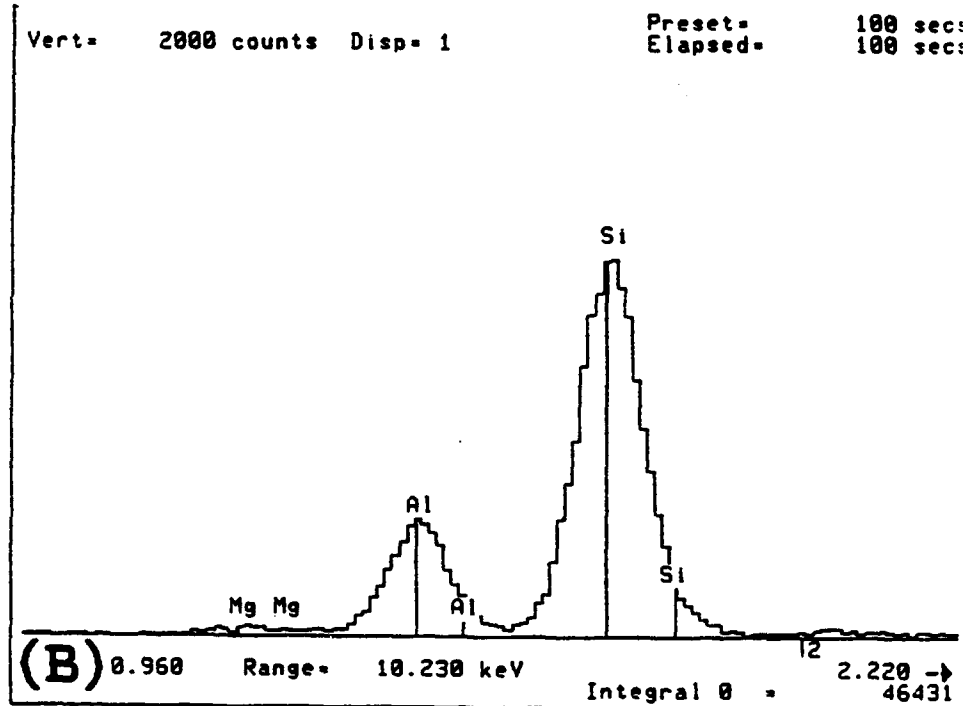
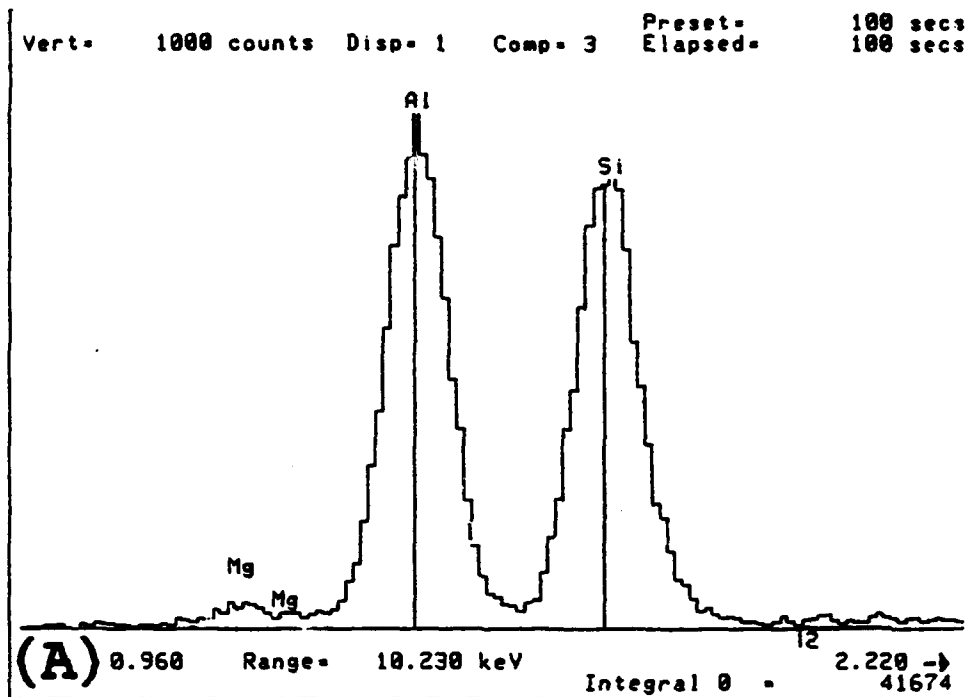
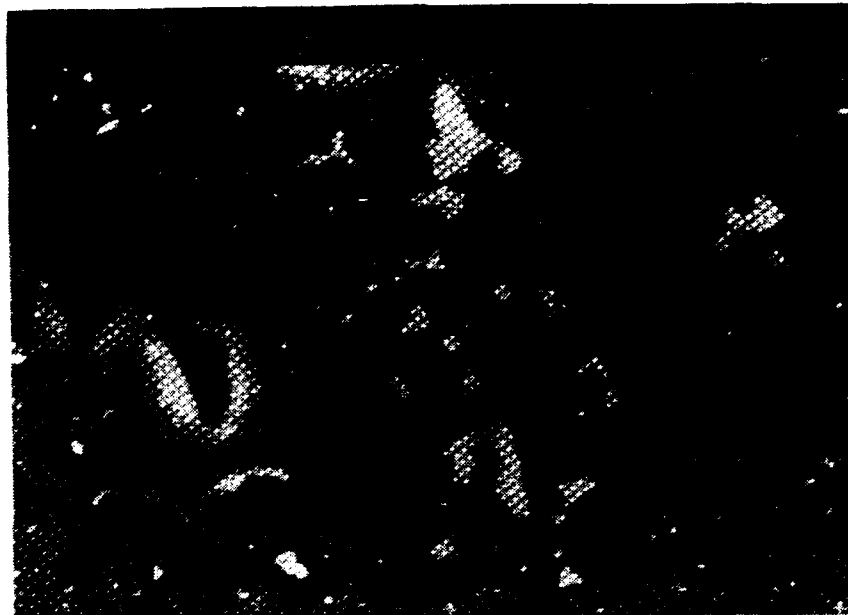


Figure 14. EDX spectra of (a) mullite phase and (b)  $\beta$ -spodumene matrix

Some areas of the matrix show the zircon phase which are approximately 2  $\mu\text{m}$  in size as shown in Figure 15. X-ray elemental maps of the zircon phase suggested a high concentration of Zr combined with Si.



**Figure 15.** High magnification BS electron image of zircon crystalline phases.

As seen under the SEM corrosion of the surface exposed to  $\text{Na}_2\text{SO}_4$  appeared to be general in nature rather than concentrated at specific microstructural features. The extent of oxygen diffusion resulting in degradation of the glass-ceramic matrix and SiC fiber is shown in Figure 16. Figure 16(a) is that of the salt-coated specimen heat-treated in flowing oxygen. Note that the fibers close to the surface were



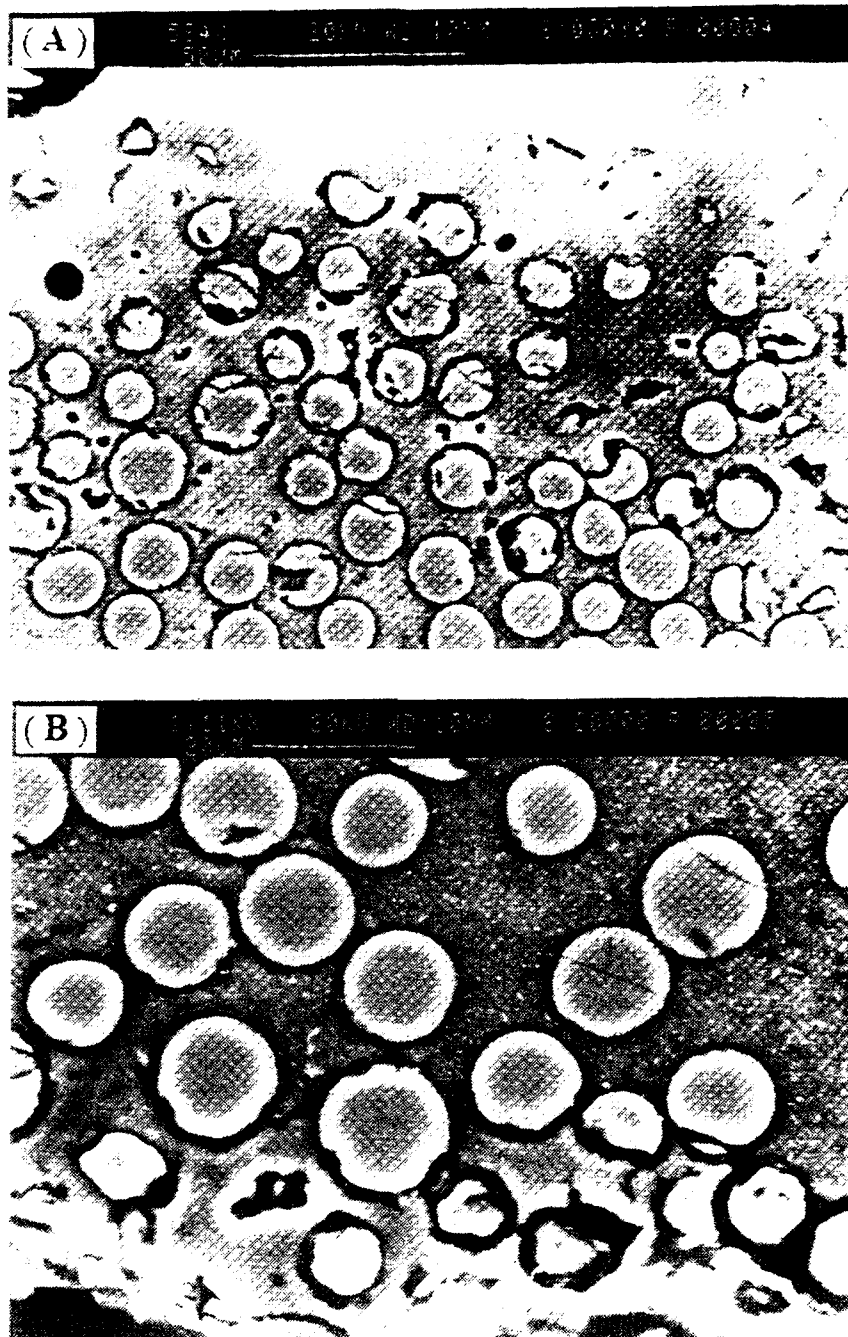
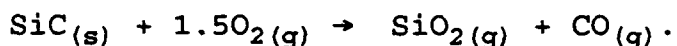
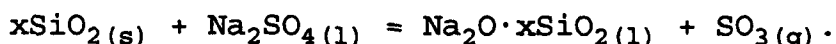


Figure 16. Comparison of extent of corrosion in samples heat-treated in oxygen. (a) Salt-coated (b) Noncoated.

completely degraded and significantly reduced in size. It appears that corrosion initiated at the fibers exposed at the surface. Also, the attack on the matrix and fiber is extensive to a depth of approximately 100  $\mu\text{m}$  from the surface. Additionally, there appears to be a lot of pores (bubbles) in the matrix. These bubbles could have arisen as a result of the oxidation of SiC fiber which yielded a large amount of CO gas in accordance with the following chemical reaction:



In comparison with Figure 16(b) which is that of the noncoated sample heat-treated in oxygen, the depth of corrosion penetration is only about 20  $\mu\text{m}$  from the surface, that is, reaction appears to be limited to the fibers exposed at the surface. These observations support what is a commonly accepted fact that  $\text{Na}_2\text{SO}_4$  in its molten state enhances the oxidation of SiC fibers by facilitating the diffusion of oxygen. The following chemical reaction applies



The protective solid  $\text{SiO}_2$  layer between the matrix and the SiC fiber is transformed into a liquid thereby reducing its viscosity. Molecular transport through the liquid is rapid resulting in accelerated attack of the SiC fiber. Also noted in the exposed surface was the significant amount of matrix cracking. The fact that the as-received sample showed no

indication of matrix cracking indicates that the presence of sodium sulfate induced matrix cracking. It was speculated in previous work of Wang, Kowalik, and Sands [Ref. 16] on Nicalon fiber-reinforced calcium aluminosilicate composites that the presence of sodium results to the formation of new phases which lead to volume changes and subsequent matrix cracking. In the present study the appearance of a distinct  $\text{MgSiO}_3$  phase and the dissolution of the mullite phase could possibly have introduced some volume change similar to that suggested by Wang, et al. Matrix cracks enhance fiber and matrix degradation by providing direct diffusion paths for oxygen.

Another interesting feature observed in the salt-coated specimen heat-treated in oxygen was the presence of distinct, well-defined  $\text{MgO} \cdot \text{SiO}_2$  phases as shown in Figure 17. X-ray elemental map obtained from EDX confirmed the presence of Mg and Si in this phase. The x-ray spectra in Figure 18 indicated a Mg atomic percent of 46.21 and Si atomic percent of 49.16 which basically is a one-to-one atomic ratio thus supporting the fact that the phase is  $\text{MgO} \cdot \text{SiO}_2$ . The  $\text{MgO} \cdot \text{SiO}_2$  phases were concentrated on areas adjacent to the salt-coated surface and none were noted in the interior of the matrix. This implies that Mg at the surface has reacted with the  $\text{SiO}_2$ . This is not surprising since diffusion rates are high in the low viscosity glassy phase. It is also possible that Mg is

diffusing from the interior to take part in this reaction but because of the small amount of Mg present it was difficult to map a concentration gradient between the interior and the surface.



**Figure 17.** Backscattered electron image of magnesium silicate phase.

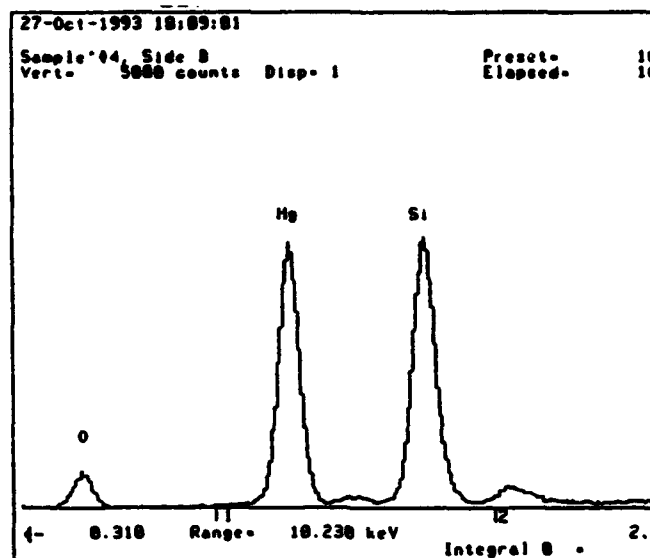


**Figure 18.** EDX X-ray spectra of  $\text{MgO} \cdot \text{SiO}_2$  phase.

Figure 19(a) is a high magnification view of an oxidized SiC fiber with a characteristic ring around it. The x-ray elemental map (Figure 19b) clearly demonstrates the segregation of the fiber, interface, and matrix. The silicon map shows the fiber appearing the brightest indicating that the concentration of Si in the fiber is much greater than the surrounding matrix. The oxygen map has an elliptical profile rather than perfectly round. This is due to the fact that the fiber is not perfectly flat and flush with the matrix surface as shown in the backscattered electron topographic image

(Figure 20). With the x-ray detector positioned at  $135^\circ$  relative to the fiber, x-ray emissions coming from the back ( $315^\circ$  relative) of the fiber are difficult to detect because they have low energy and are readily absorbed by the protruding fiber. These studies clearly suggest that the original interface between the SiC and the matrix have been destroyed and that the significant amounts of the fibers have been oxidized to form  $\text{SiO}_2$  which appears to be the dominant phase in the 'rings' described above.

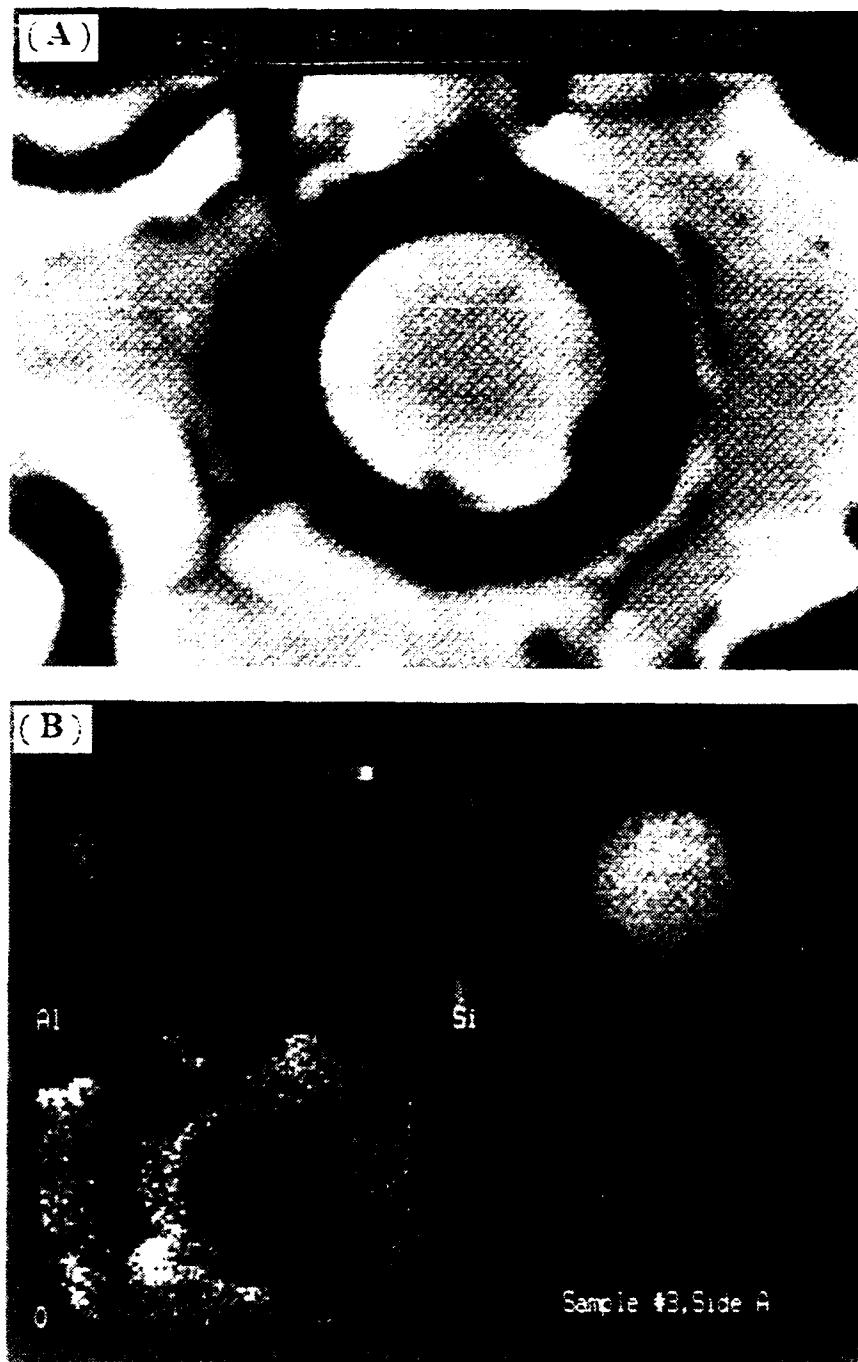


Figure 19. Oxidized SiC fiber. (a) Secondary electron SEM image (b) X-ray elemental map.



**Figure 20.** Backscattered electron topographic image of SiC fiber and matrix.

The salt-coated side of the test coupon heat treated in argon is shown in Figure 21(a). Fiber degradation appears to be limited to the fibers exposed at the surface and consequently are in direct contact with the  $\text{Na}_2\text{SO}_4$  salt. Note that there is also a magnesium silicate phase formed at the surface. Figure 21(b) shows the noncoated specimen heat treated in argon. There is virtually no noticeable difference in fiber and matrix surface morphologies between this sample and those of the as-received specimen except for the disappearance of the mullite needles.



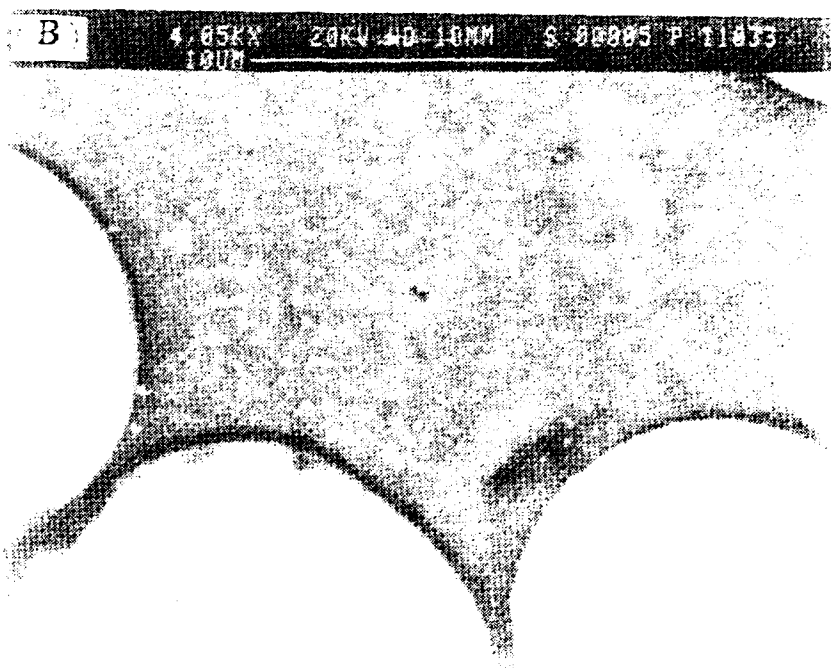
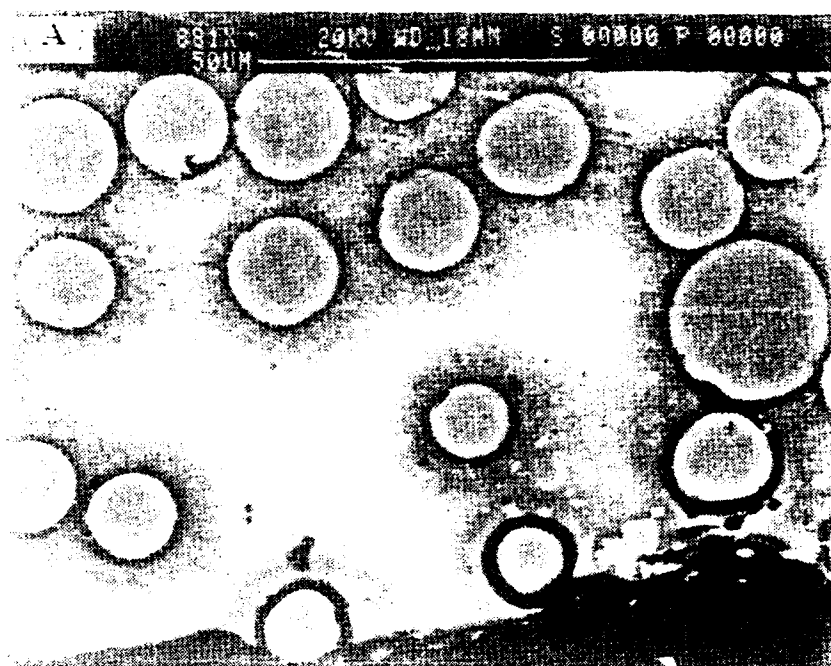


Figure 1. SEM images of (A) a field of cells and (B) a single cell.

It should be noted that trace amount of Na was observed in the raw EDX spectra of the samples coated with sodium sulfate. It was difficult to detect Na because only small amount was present such that no meaningful quantitative analysis could be obtained from the EDX spectra. Similarly, the XRD patterns did not reveal crystallographic phases that could confirm the presence of sodium.

#### **A. X-RAY DIFFRACTION (XRD) ANALYSIS**

The as-received and heat-treated samples were analyzed using X-ray diffraction in order to determine the crystalline phases present and any changes therein resulting from the heat treatment and exposure to sodium sulfate. Figure 22 illustrates the x-ray diffraction patterns of the crystalline phases in the as-received sample. All the distinguishable intensity peaks and line positions were identified by using the Phillips APD1700 software package in conjunction with the Hanawalt JCPD diffraction patterns data cards. The Miller indices were obtained from X-ray Diffraction Data Cards published by the Joint Committee on Chemical Analysis by X-ray Diffraction Methods (October 1955 copyright by the American Society for Testing Materials). In cases where the relative intensities were identical, such as in mullite where the relative intensity of 50 corresponded to either (110) or (111)

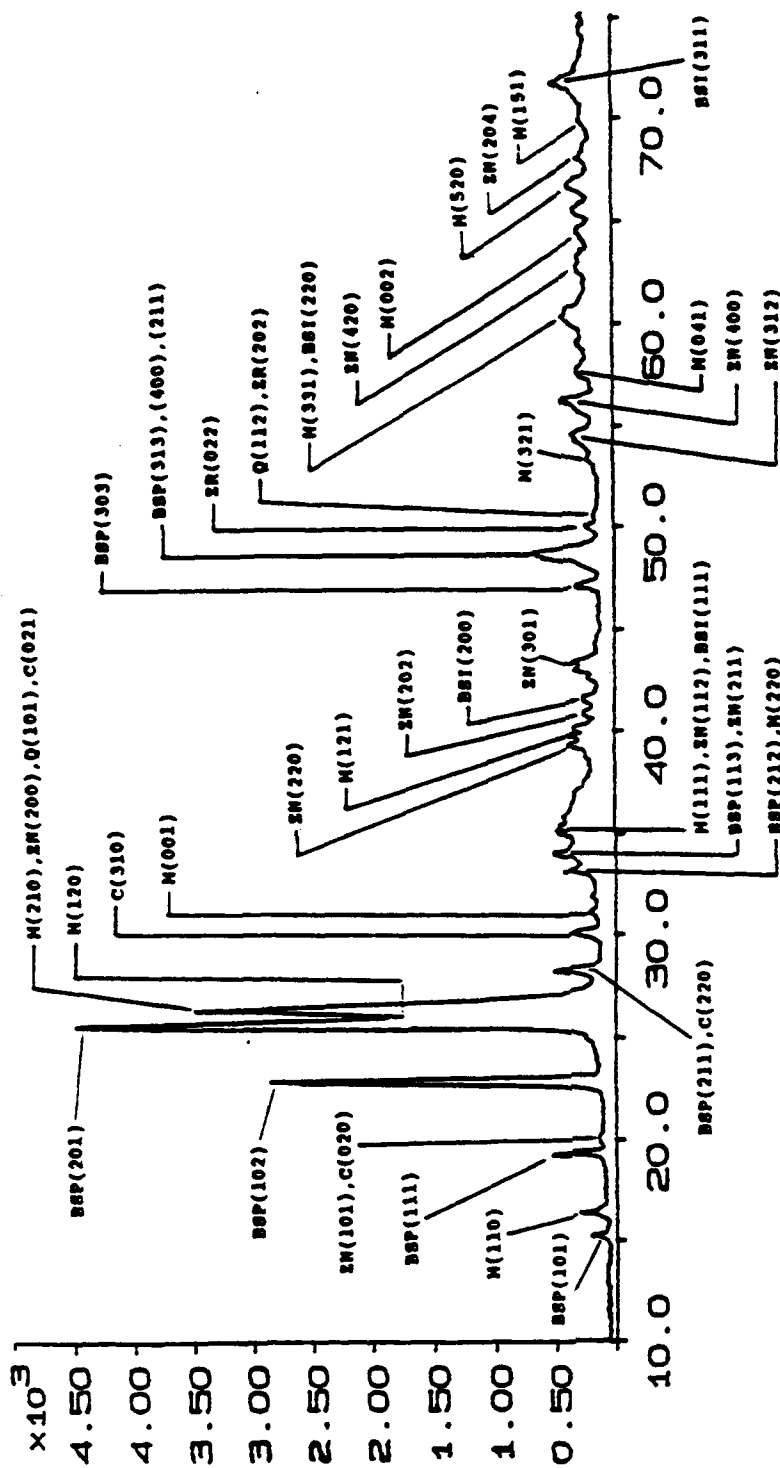


Figure 22. X-ray diffraction patterns of the as-received specimen showing the crystalline phases present and corresponding Miller indices. BSP =  $\beta$ -spodumene, BSI =  $\beta$ -SiC, M = mullite, Q = quartz, ZN = zircon, ZR = zirconia, C = clinoenstatite.

peaks, Bragg's Law (  $\lambda = 2d\sin\theta$  ) was used to differentiate the two peaks. Since the wavelength (  $\lambda$  ) of the x-ray used and the  $2\theta$  where the peak occurs are both known, the interplanar spacing (d) can be calculated. Once the value of d is known, the Miller indices can be easily determined from the XRD Data Cards.

$\beta$ -spodumene solid solution was the main crystalline phase present as evidenced by the most intense (201) peak at  $2\theta$  equal to  $25.5^\circ$ . The  $\beta$ -spodumene (102), (111), and (101) peaks at  $2\theta$  equal to  $22.5^\circ$ ,  $19.0^\circ$ , and  $15.2^\circ$ , respectively, further confirm the presence of  $\beta$ -spodumene. No other crystalline phases present in this particular matrix have peaks at those  $2\theta$  values. However, lithium aluminosilicate has several polymorphs two of which are illustrated in Figure 23. The diffraction patterns of  $\text{LiAlSi}_2\text{O}_6$  and  $\text{LiAlSi}_3\text{O}_8$  are almost identical. But based on the phase diagram (Figure 1),  $\text{LiAlSi}_2\text{O}_6$  ( $\beta$ -spodumene) must be the phase present in the matrix since  $\text{LiAlSi}_3\text{O}_8$  is not one of the crystalline phases expected.

Other phases present in the matrix are mullite ( $3\text{Al}_2\text{O}_3 \cdot 2\text{SiO}_2$ ), zircon ( $\text{ZrO}_2 \cdot \text{SiO}_2$ ), zirconia ( $\text{ZrO}_2$ ), quartz ( $\text{SiO}_2$ ), and clinoenstatite ( $\text{MgSiO}_3$ ). The tetragonal polymorph of zirconia is the most likely phase present because the

orthorhombic form is a high pressure phase. The presence of clinoenstatite is not evident in the as-received sample, but the SEM and XRD analyses of the salt-coated sample heat-treated in oxygen show strong evidence for clinoenstatite. For the given weight percentage composition of lithia, alumina, and silica provided in TABLE I, the presence of  $\beta$ -spodumene and mullite is in agreement with the ternary phase diagram shown in Figure 24. In addition to the matrix crystalline phases noted, the characteristic silicon carbide (111), (200), (220), and (311) peaks at  $2\theta$  equal to  $35.8^\circ$ ,  $41.5^\circ$ ,  $60.0^\circ$ , and  $71.8^\circ$ , respectively, were also observed in the XRD spectra of the as-received specimen. However, it was difficult to determine from XRD data alone (Figure 25) whether the silicon carbide phase is either  $\alpha$ -SiC or  $\beta$ -SiC. However, previous work [Ref. 21] by electron diffraction has shown that these fibers are predominantly  $\beta$ -SiC.

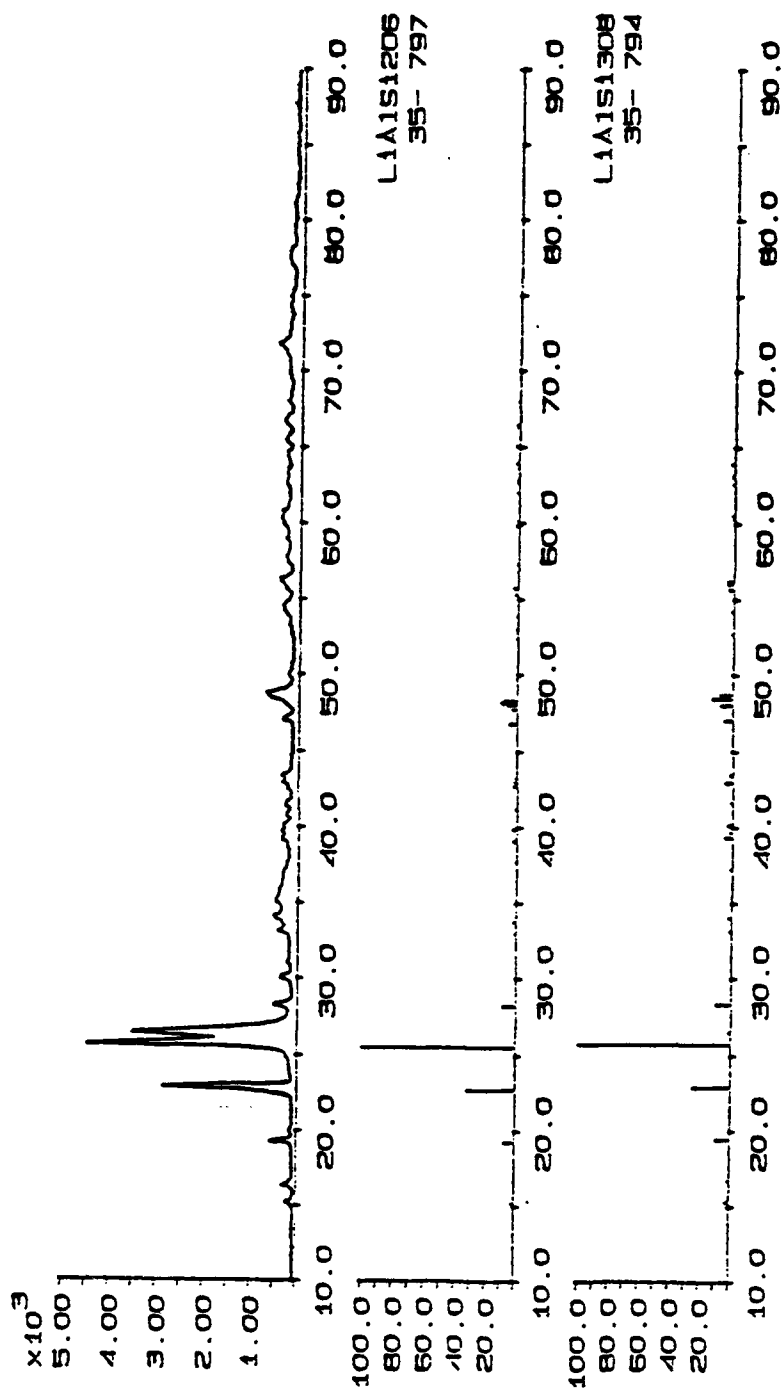


Figure 23. Comparison of diffraction patterns of as-received sample and two lithium aluminosilicate polymorphs:  $\text{LiAlSi}_2\text{O}_8$  and  $\text{LiAlSi}_3\text{O}_8$ .

$\text{Li}_2\text{O}-\text{Al}_2\text{O}_3-\text{SiO}_2$

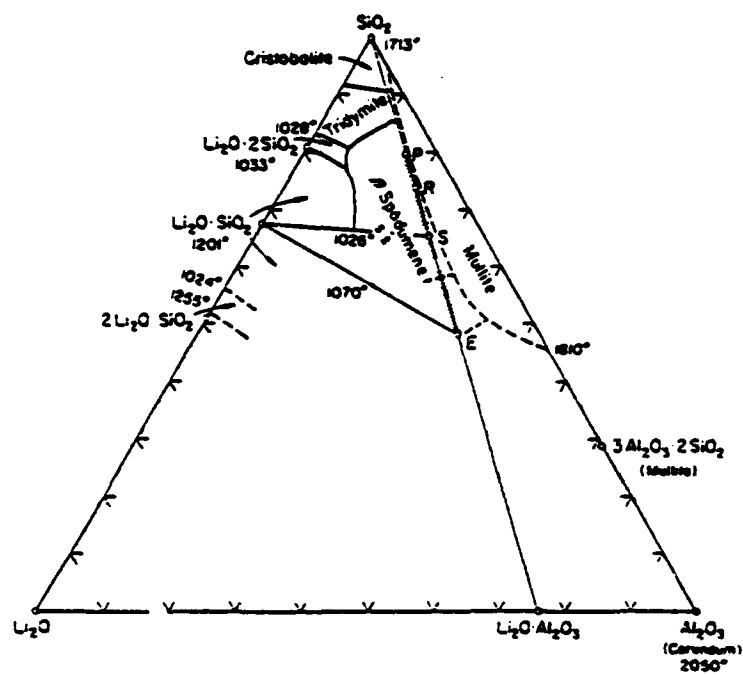


Figure 24.  $\text{Li}_2\text{O}-\text{Al}_2\text{O}_3-\text{SiO}_2$  ternary phase diagram.

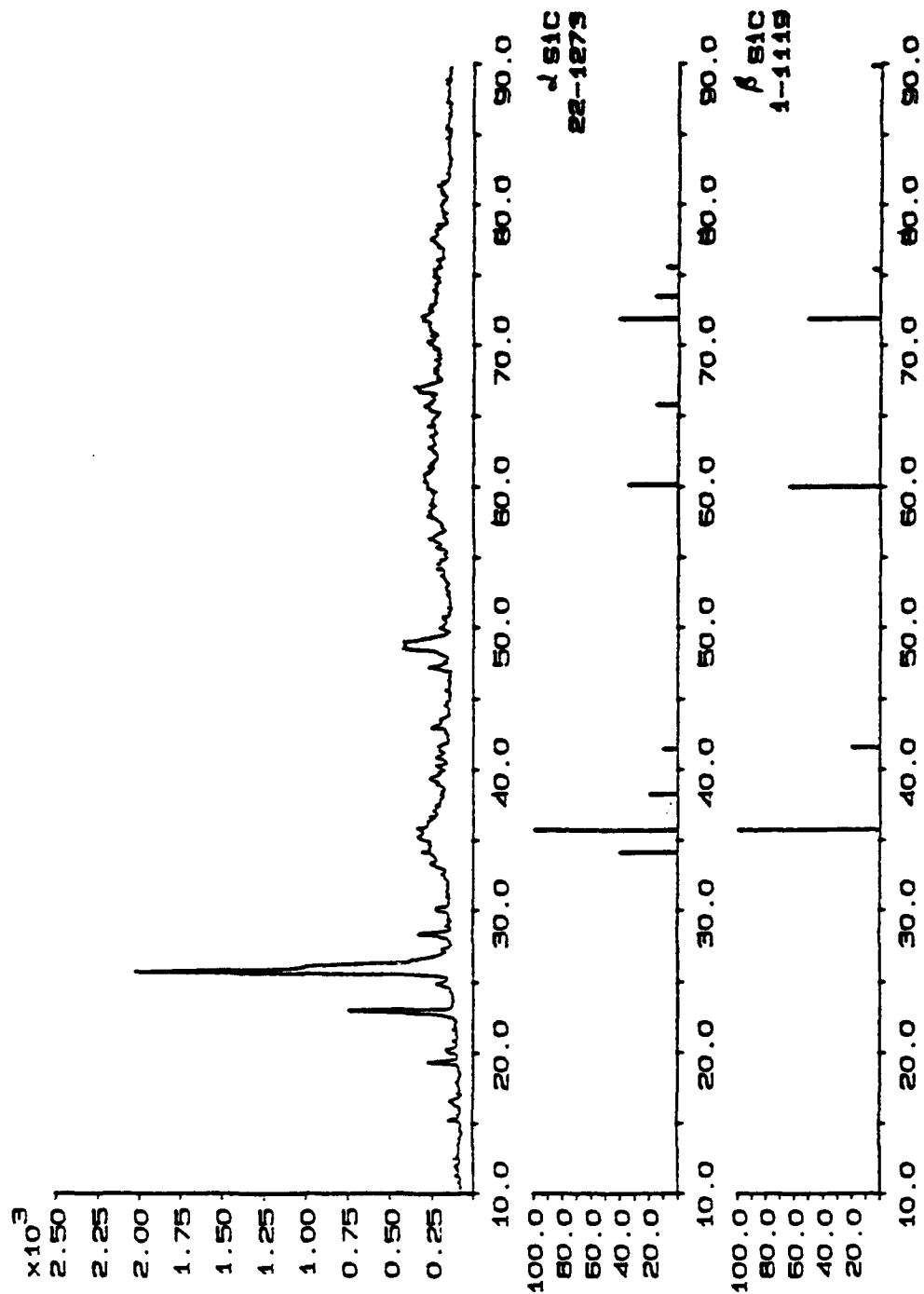


Figure 25. Comparison of diffraction patterns of as-received sample and two SiC polymorphs:  $\alpha$ -SiC and  $\beta$ -SiC.



TABLE II shows the crystalline phases present, relative intensities of the three strongest lines in the diffraction pattern of each phase, Miller indices, and the  $2\theta$  location of the peaks in the diffraction pattern of the as-received sample.

TABLE II. PHASES PRESENT, RELATIVE INTENSITIES, MILLER INDICES, AND LINE POSITIONS ( $2\theta$ ) IN AS-RECEIVED SPECIMEN.

PHASES	RELATIVE INTENSITIES	MILLER INDICES(hkl)	$2\theta$ (degrees)
$\beta$ -spodumene (Tetragonal)	100	(201)	25.5
	32	(102)	22.5
	10	(400)	48.7
Mullite (Orthorhombic)	100	(210)	26.5
	95	(120)	26.0
	50	(110)	16.8
$\beta$ -SiC (Cubic)	100	(111)	35.8
	63	(220)	60.0
	50	(311)	71.8
Zircon (Tetragonal)	100	(200)	26.9
	45	(112)	35.6
	45	(101)	20.0
Zirconia (Tetragonal)	100	(111)	30.1
	22	(202)	50.2
	20	(022)	49.8
Quartz (Hexagonal)	100	(101)	26.5
	22	(100)	20.8
	14	(112)	50.1
Clinoenstatite (Monoclinic)	100	(100)	31.7
	69	(221)	30.7
	47	(220)	28.2

Figure 26 and 27 illustrate the X-ray diffraction patterns of the as-received and heat-treated samples. It is apparent that heat treatment either in oxygen or in argon has an important effect on the crystalline phases particularly on the mullite phase. The salt-coated specimen heat-treated in oxygen shows the mullite (210) and (120) peaks at  $2\theta$  equal to  $26.5^\circ$  and  $26.0^\circ$ , respectively, are significantly reduced. The decrease in mullite peaks suggests that it dissolved and coprecipitated with the glassy phase. The SEM results support the fact that the mullite disappeared. Figure 28 is a comparison of backscattered electron micrographs of the as-received and heat-treated (in argon, no salt coating) specimens. Particularly noteworthy from the micrographs is the fact that the needle-like, light-colored mullite phases clearly present in the as-received sample are not present in the heat-treated samples. This also applies to the other three heat-treated test pieces. Previous studies by Xue and Chen on mullite fabrication [Ref. 19] demonstrated that mullite crystal formation occurred at  $1400^\circ\text{C}$  and continued to increase with increasing heat treatment temperature. In the present study it is speculated that the mullite which formed during the hot pressing process ( $1250^\circ\text{C}$ ) reverted back to a glassy phase during heat treatment at a much lower temperature

(900 °C) or it could have changed the composition of the crystalline  $\beta$ -spodumene.

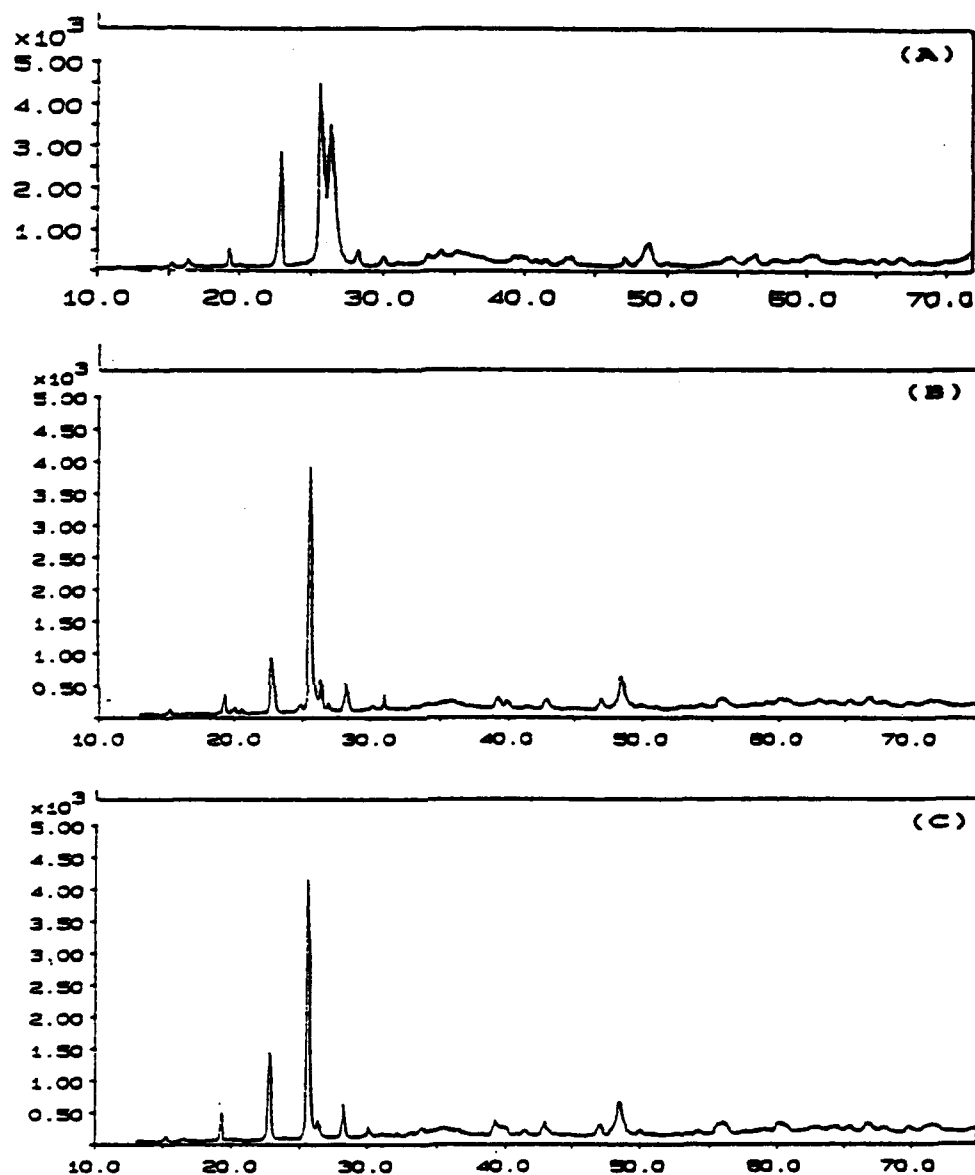


Figure 26. Comparison of XRD patterns of (a) as-received, (b) salt-coated, heat-treated in oxygen, and (c) noncoated, heat-treated in oxygen.

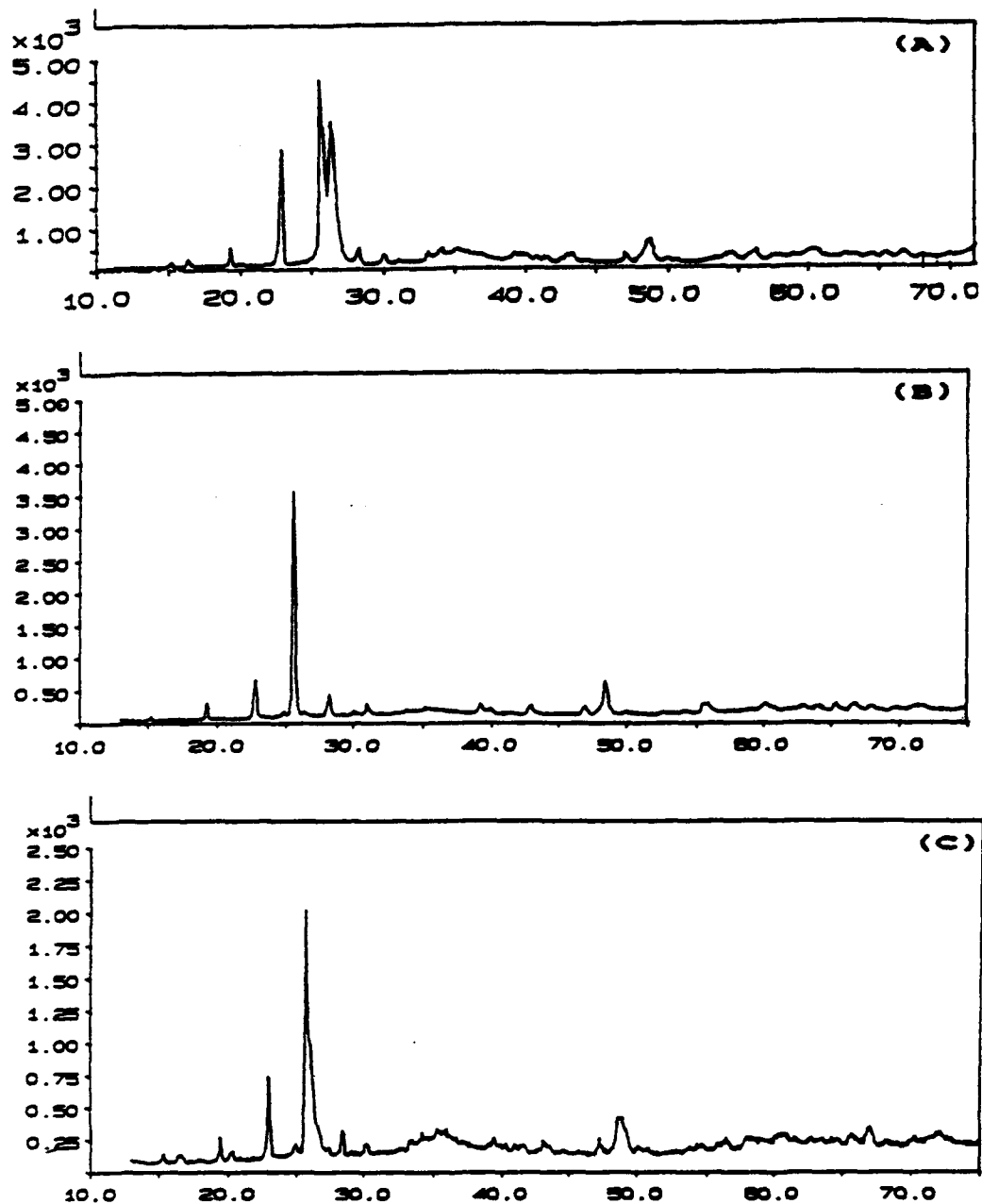


Figure 27. Comparison of XRD patterns of (a) as-received, (b) salt-coated, heat-treated in argon, and (c) noncoated, heat-treated in argon.

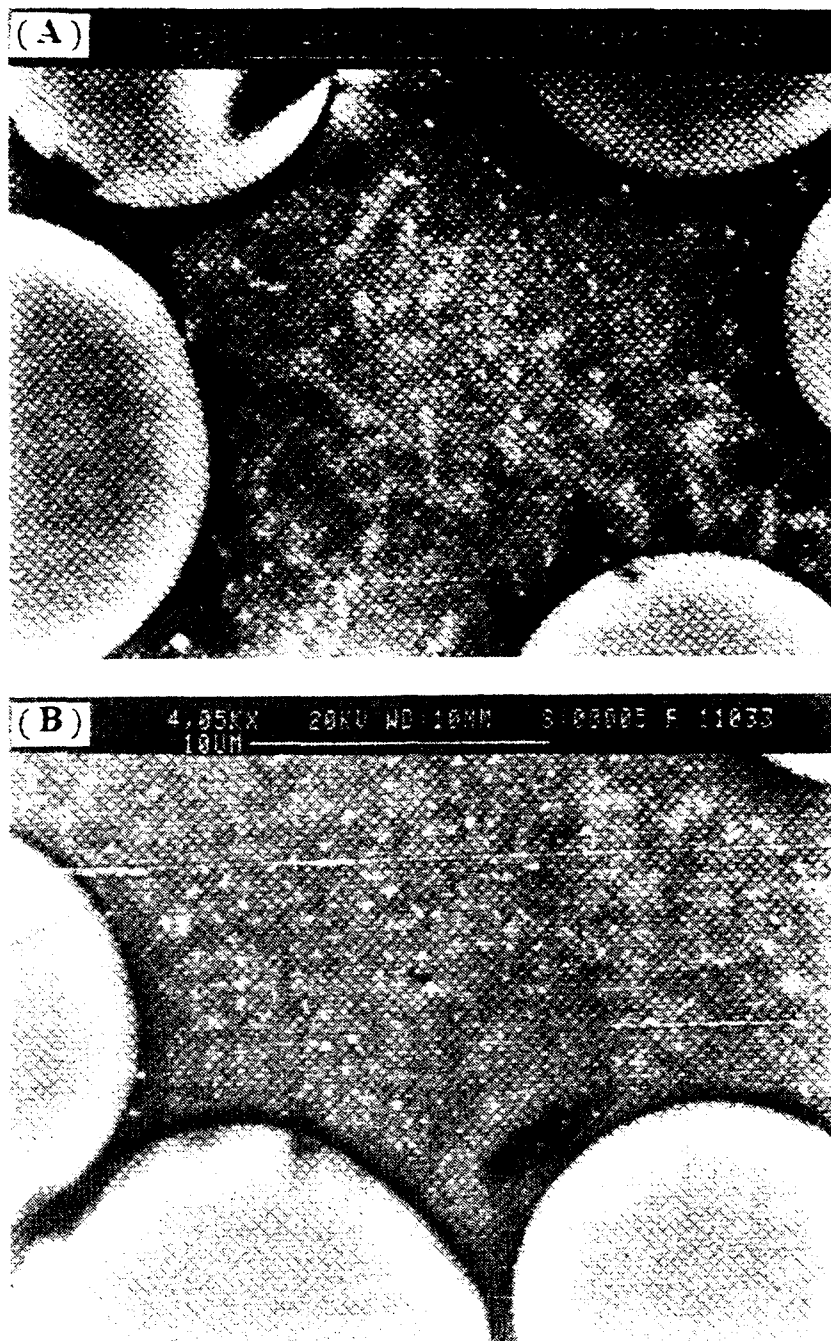


Figure 28. BS electron image of (a) as-received and (b) heat-treated specimens showing the changes in microstructures.

Another interesting feature observed in the x-ray diffraction patterns of the salt-coated, heat-treated (in oxygen) specimen is the presence of two distinct peaks at  $2\theta$  equal to  $20.0^\circ$  and  $20.5^\circ$ . The as-received sample only shows a single hump over these  $2\theta$  values. The two new peaks correspond to the (020) and (011) peaks of clinoenstatite ( $\text{MgO} \cdot \text{SiO}_2$ ). The other three heat-treated specimens do not display these two peaks. The presence of clinoenstatite in lithium aluminosilicate glass-ceramics having magnesium oxide as one of its constituents has been confirmed in previous work by Peinan, Jingkun, et. al [Ref. 18]. As discussed previously in the SEM results section, the presence of molten sodium silicate in an oxidizing environment causes the enhanced diffusion of MgO towards the salt-coated surface which results in the formation of magnesium silicate ( $\text{MgO} \cdot \text{SiO}_2$ ).

Comparing the relative peak heights of  $\beta$ -spodumene peaks in the as-received sample and those of the heat-treated specimens, it is evident that there is a slight decrease in  $\beta$ -spodumene peak intensities resulting from the heat treatment. TABLE III presents a comparison of  $\beta$ -spodumene relative peak heights between the as-received and a heat-treated sample. This suggests that the heat treatment has led to increased glassiness, although the samples used were slightly smaller for the heat-treated samples.

**TABLE III. SELECTED  $\beta$ -SPODUMENE PEAK INTENSITIES IN AS-RECEIVED AND SALT-COATED HEAT-TREATED IN OXYGEN SPECIMENS**

$2\theta$ (degrees)	MILLER INDICES (hkl)	AS- RECEIVED (counts)	HEAT- TREATED (counts)
25.5	(201)	4525	3850
22.5	(102)	2990	920
19.0	(111)	550	350
15.2	(101)	210	150

Although the dominant mullite (210) peak at  $2\theta$  equal to  $26.5^\circ$  disappeared due to the heat treatment, there still remains a weak but rather distinct peak at that location. It is most likely that the peak is due to the formation of crystalline quartz. Hexagonal low quartz has its most intense (101) peak located also at  $26.5^\circ$  (see TABLE II) and no other  $\text{SiO}_2$  polymorph has a 100% peak at this location. The reaction between SiC and  $\text{Na}_2\text{SO}_4$  yields a glassy product and XRD analyses performed by Federer on SiC ceramics exposed to  $\text{Na}_2\text{SO}_4$  vapor at  $1200^\circ\text{C}$ . [Ref. 20] indicated that this glassy product is a silica glass containing quartz as one of the crystalline phases. Comparison of the quartz (101) peaks in the XRD patterns of the four heat-treated samples shows that the salt-coated sample heat-treated in oxygen has the most intense peak relative to the other three. This should be

expected since there would be more silica glass, and thus more quartz, produced in the presence of  $\text{Na}_2\text{SO}_4$  and oxygen in both the matrix and in the  $\text{SiO}_2$  rings surrounding the corroded fibers.



## VI. CONCLUSIONS

Results of this study on the effects of sodium sulfate salt corrosion of SiC fiber-reinforced LAS glass-ceramic composites indicate the following:

- Corrosion of SiC/LAS composite is most extensive in the presence of sodium sulfate salt and oxygen.
- Corrosion is limited to the fibers and matrix exposed at the surface in noncoated sample heat-treated in oxygen and in salt-coated sample heat-treated in argon. This and the observation stated above imply that sodium sulfate and oxygen must be both present for severe corrosion to occur.
- Fibers and matrix in noncoated sample heat-treated in argon are microstructurally similar to the as-received sample except for the disappearance of mullite.
- Heat treatment apparently causes the dissolution of mullite into either the glassy phases or  $\beta$ -spodumene crystalline phase.
- The presence of  $\text{MgSiO}_3$  in the salt-coated sample heat-treated in oxygen implies that Mg at the surface reacted with  $\text{SiO}_2$ . Molecular diffusion is enhanced by the low viscosity of the glassy phase caused by the reaction with the molten sodium sulfate.
- These results are consistent with the tensile test data of Wang, Kowalik, and Sands [Ref. 16] shown in Figure 10 which indicates that simple heat treatment of SiC/LAS without salt in argon did not affect tensile strength very much, but that annealing in air with a  $\text{Na}_2\text{SO}_4$  coating severely degraded properties.

## VII. RECOMMENDATIONS

Since the interface between the SiC fiber and the glass-ceramic matrix plays an important role in determining the strength and toughness of the composite, a Transmission Electron Microscopy (TEM) analysis of the interface should be conducted. Because the fiber-matrix interface is only 70-170 nm wide in the as-received sample conclusive information could not be obtained from SEM and XRD analyses.

B<sub>2</sub>O<sub>3</sub> was incorporated with the matrix in order to form a boron/carbon interface which should reduce the oxidation of the SiC fiber [Ref. 10]. Specimens with and without B<sub>2</sub>O<sub>3</sub> should be examined to determine the effectiveness of B<sub>2</sub>O<sub>3</sub> in retarding SiC fiber oxidation.

Since the oxidation of the SiC fibers is preceded by the degradation of the normally protective SiO<sub>2</sub> layer, Federer [Ref. 20] suggested a possible solution to the corrosion problem by coating the SiC fibers with a more refractory compound like alumina (Al<sub>2</sub>O<sub>3</sub>). The melting temperature of Na<sub>2</sub>O·Al<sub>2</sub>O<sub>3</sub>·2SiO<sub>2</sub> (22 wt.% Na<sub>2</sub>O, 36 wt.% Al<sub>2</sub>O<sub>3</sub>, and 42 wt.% SiO<sub>2</sub>) is ~1525 °C whereas Na<sub>2</sub>O·SiO<sub>2</sub> is all liquid at 1200 °C. Other coating compounds recommended were Cr<sub>2</sub>O, MgO, TiO<sub>2</sub>, and ZrO<sub>2</sub>. Applications of the aforementioned compounds as fiber

coating should be further investigated to determine their effectiveness in either preventing or minimizing SiC fiber corrosion.

## LIST OF REFERENCES

1. Z. Strnad, "Glass Ceramics Materials", 1986.
2. D.R. Askeland, The Science and Engineering of Materials, PWS-Kent Publishing Co., 1989.
3. K.M.Prewo, "Tension and Flexural Strength of Silicon Carbide Fiber-reinforced Glass Ceramics", Vol. 21, p. 3590, 1986.
4. K.M.Prewo and J.J.Brennan, "Gas Turbine Engine and Composite Parts", United Technologies Research Corporation, Patent No. 4,626,461, December 1986.
5. J. Hsu and R.F. Speyer, "Fabrication and Properties of SiC Fiber-reinforced  $\text{Li}_2\text{O}\cdot\text{Al}_2\text{O}_3\cdot 6\text{SiO}_2$  Glass-Ceramic Composites", Journal of Materials Science, Vol. 27, p. 381, 1992.
6. J. Hsu and R.F. Speyer, "Interfacial Phenomology Of SiC Fiber-reinforced  $\text{Li}_2\text{O}\cdot\text{Al}_2\text{O}_3\cdot 6\text{SiO}_2$  Glass-Ceramic Composites", Journal of Materials Science, Vol. 27, p. 374, 1992.
7. B.E. Deal and A.S. Grove, "General Relationships for Thermal Oxidation of Silicon", Journal of Applied Physics, Vol. 36, No. 12, p. 3770, 1965.
8. N.S. Jacobson, "Corrosion of Silicon-Based Ceramics in Combustion Environments", Journal of American Ceramic Society, Vol. 76, No. 1, p. 3, 1993.
9. N.S. Jacobson, "Sodium Sulfate: Deposition and Dissolution of Silica", Oxidation Metallurgy, Vol. 31, Nos. 1/2, p. 91, 1989.
10. R.W. Kowalik, S-W. Wang, and R.R.Sands, "Hot Corrosion of Nicalon Fiber-reinforced Glass-Ceramic Matrix Composites: Microstructural Effects", Naval Air Warfare Center Technical Report, Warminster, PA, 1992.

11. S.R. Saunders and T.B. Gibbons, "Developments in Test Procedures for Hot-Salt Corrosion of Superalloys", High Temperature Surface Interactions, 68th Meeting of Structures and Materials Panel of AGARD in Ottawa, Canada, 23-28 April 1989.
12. M.H. Loretto, "Electron Beam Analysis of Materials", Chapman and Hall Ltd., 1984.
13. R. Chaim and A.H. Heuer, "The Interface Between (nicalon) SiC Fiber and a Glass-Ceramic Matrix", Advanced Ceramic Materials, Vol. 2, No. 2, p. 154, 1987.
14. C. Cantalini and M. Pelino, "Characterization of Crystal Phases, Morphology and Crystallization Processes in Lithium Aluminosilicate Glass-Ceramic", Journal of Material Science, Vol. 27, p. 448, 1992.
15. J.J. Mecholsky, American Ceramic Bulletin, Vol. 68, p. 367, 1988.
16. S-W. Wang, R.W. Kowalik, and R. Sands, "Hot Corrosion of Two Nicalon Fiber-reinforced Glass-Ceramic Matrix Composites", Ceramic Engineering and Science Proceeding, Vol. 13, Nos. 7-8, p. 760, 1992.
17. N.J. Shaw, et al., "Materials for Engine Applications Above 3000°F - An Overview", NASA Report No. TM-100169, NASA Lewis Research Center, Cleveland, OH, 1987.
18. Z. Peinan, et al., "Microstructures and Properties of SiC Fibre-reinforced Glass-Ceramic Composite", Journal of Material Science Letter, Vol. 12, p. 526, 1993.
19. L.A. Xue and I-W. Chen, "Fabrication of Mullite Body Using Superplastic Transient Phase", Journal of American Ceramic Society, Vol. 75, No. 5, p. 1086, 1992.
20. J.I. Federer, "Corrosion of SiC Ceramics by Na<sub>2</sub>SO<sub>4</sub>", Advanced Ceramic Materials, Vol. 3, No. 1, p. 60, 1988.
21. J.J. Brennan, "Interfacial Studies of Refractory Glass-Ceramic Matrix/Advanced SiC Fiber Reinforced Composites", United Technologies Research Center, Report No. R93-918246-6, p. 10, 1993.

22. K.S. Siskind, "Glass-Ceramic Matrix Composites for Advanced Gas Turbine", AIAA/SAE/ASME/ASEE 26th Joint Propulsion Conference in Orlando, FL, 16-18 July, 1990.

### INITIAL DISTRIBUTION LIST

- |    |   |   |
|----|---|---|
| 1. | Defense Technical Information Center<br>Cameron Station<br>Alexandria, Virginia 22304-6145  | 2 |
| 2. | Professor M.D. Kelleher, Code ME/Kk<br>Chairman<br>Department of Mechanical Engineering<br>Naval Postgraduate School<br>Monterey, CA 93943-5000 | 1 |
| 3. | Professor Alan G. Fox, Code ME/Fx<br>Mechanical Engineering Department<br>Naval Postgraduate School<br>Monterey, CA 93943-5000                  | 2 |
| 4. | Curricular Officer, Code 34<br>Department of Naval Engineering<br>Naval Postgraduate School<br>Monterey, CA 93942-5000                          | 1 |
| 5. | LT Leopoldo C. Maldia, USN<br>11347 April Leigh Terrace<br>San Diego, CA 92123  | 5 |
| 6. | Dr. Shaio-Wen Wang<br>Code 6063<br>Aircraft Division<br>Naval Air Warfare Center<br>Warminster, PA 18974  | 1 |
| 7. | Library, Code 52<br>Naval Postgraduate School<br>Monterey, Ca 93943-5002  | 1 |